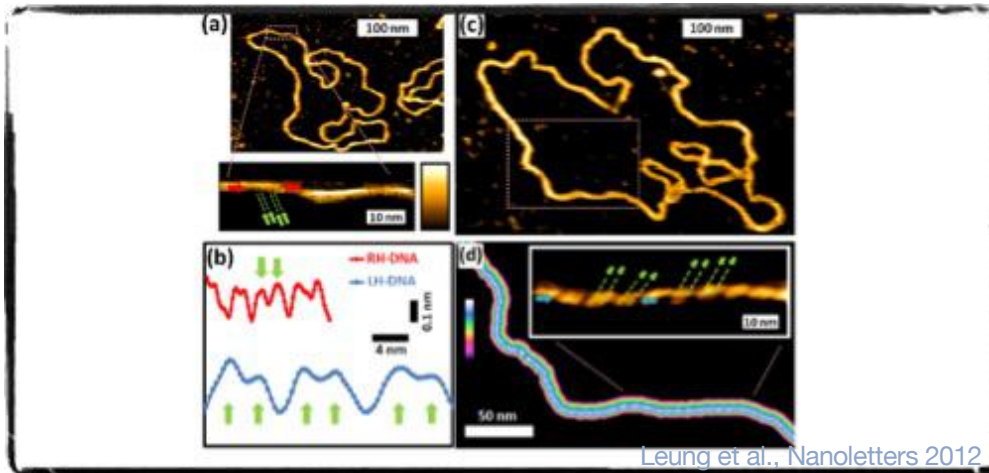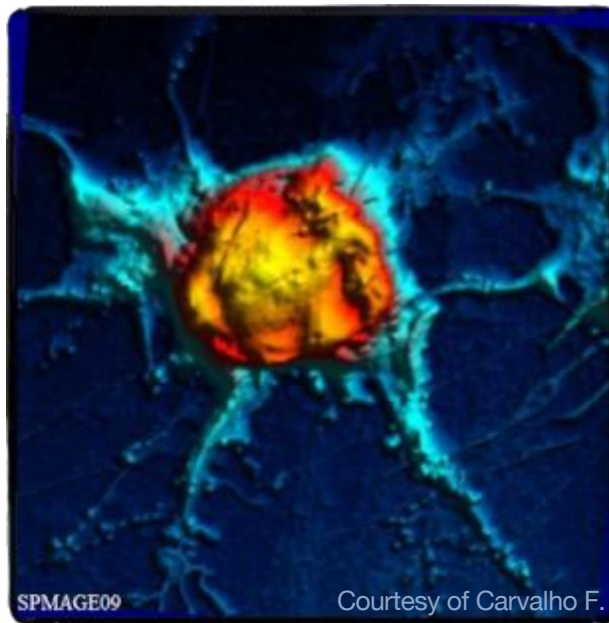# High Res/High Speed
AFM

AFM in Biology
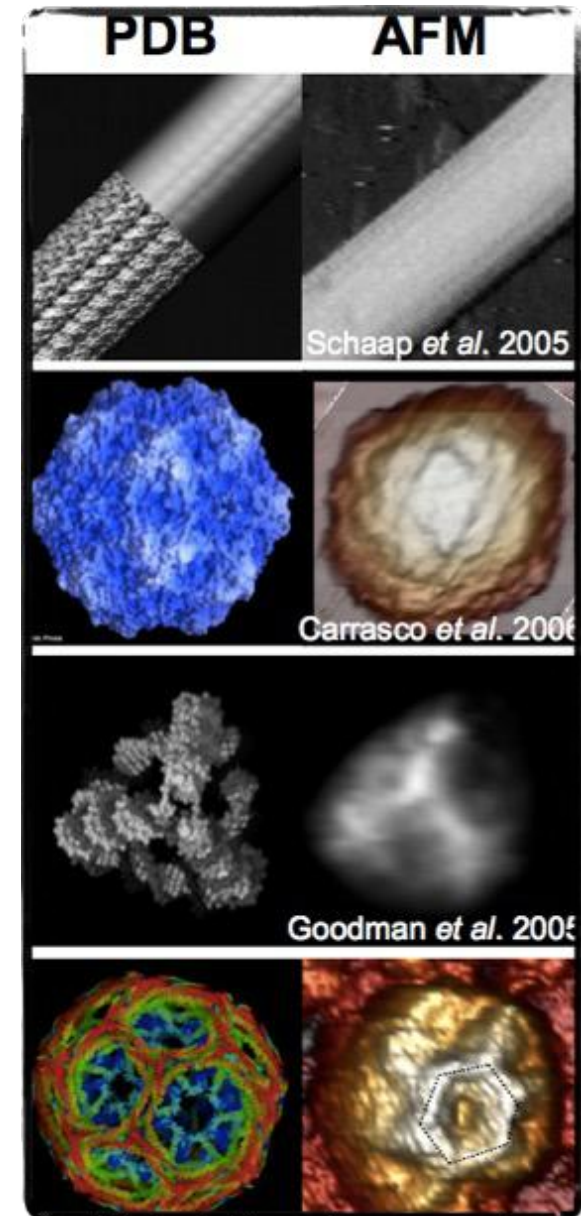
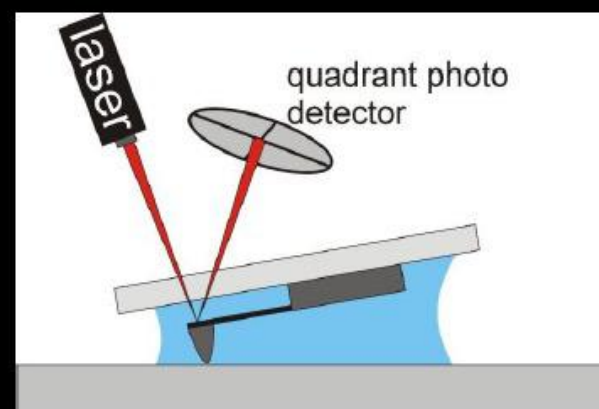## DNA

Leung et al., Nanoletters 2012

Cells

SPMAGE09

Courtesy of Carvalho F.

Proteins

PDB | AFM

Schaap et al. 2005

Carrasco et al. 2006

Goodman et al. 2005

bio-molecules: working in liquid

Clare Waterman, NIH

laser

quadrant photo detector
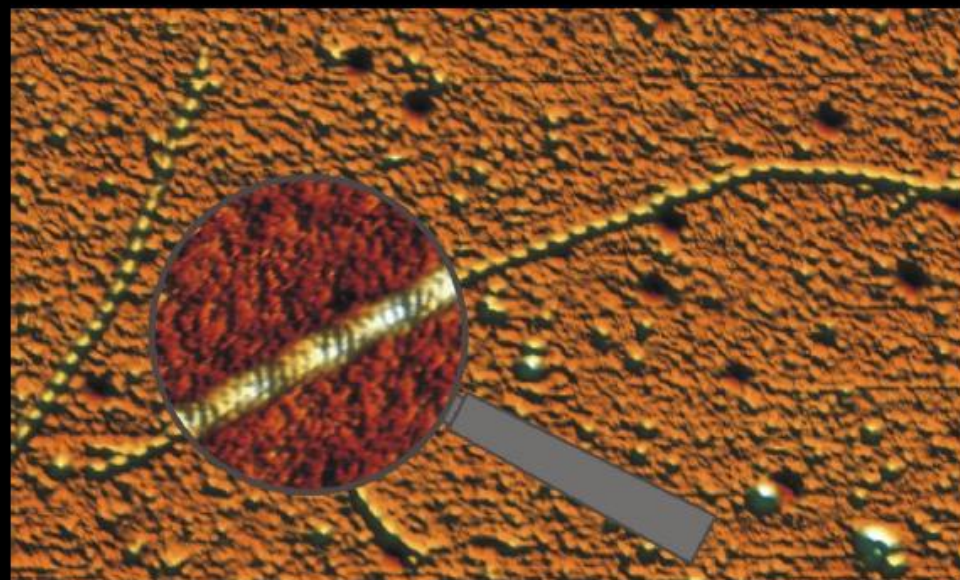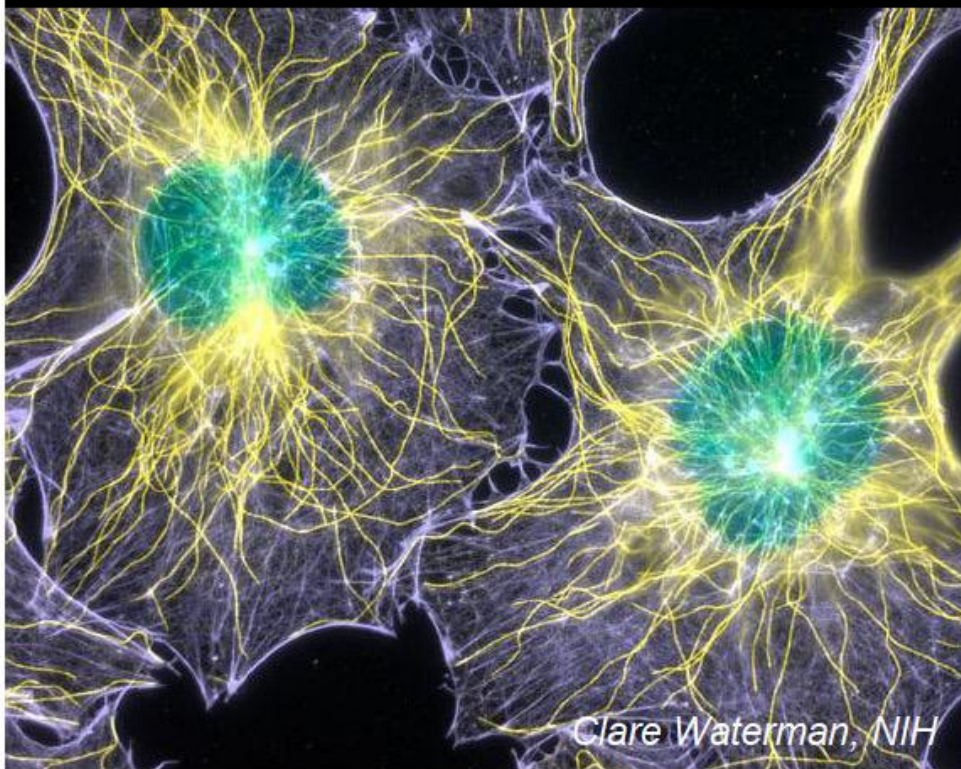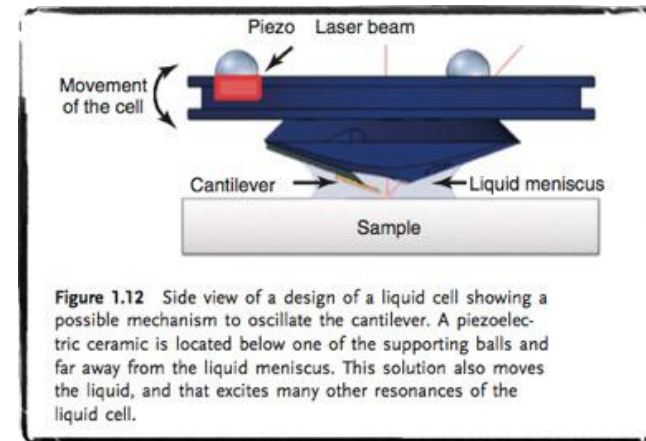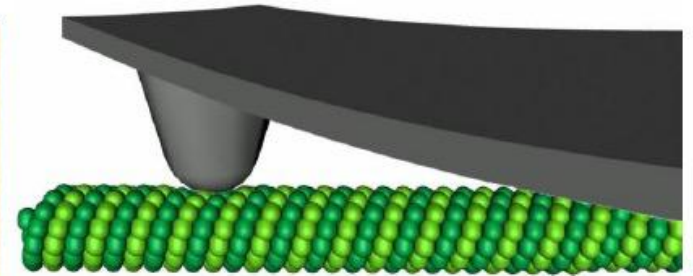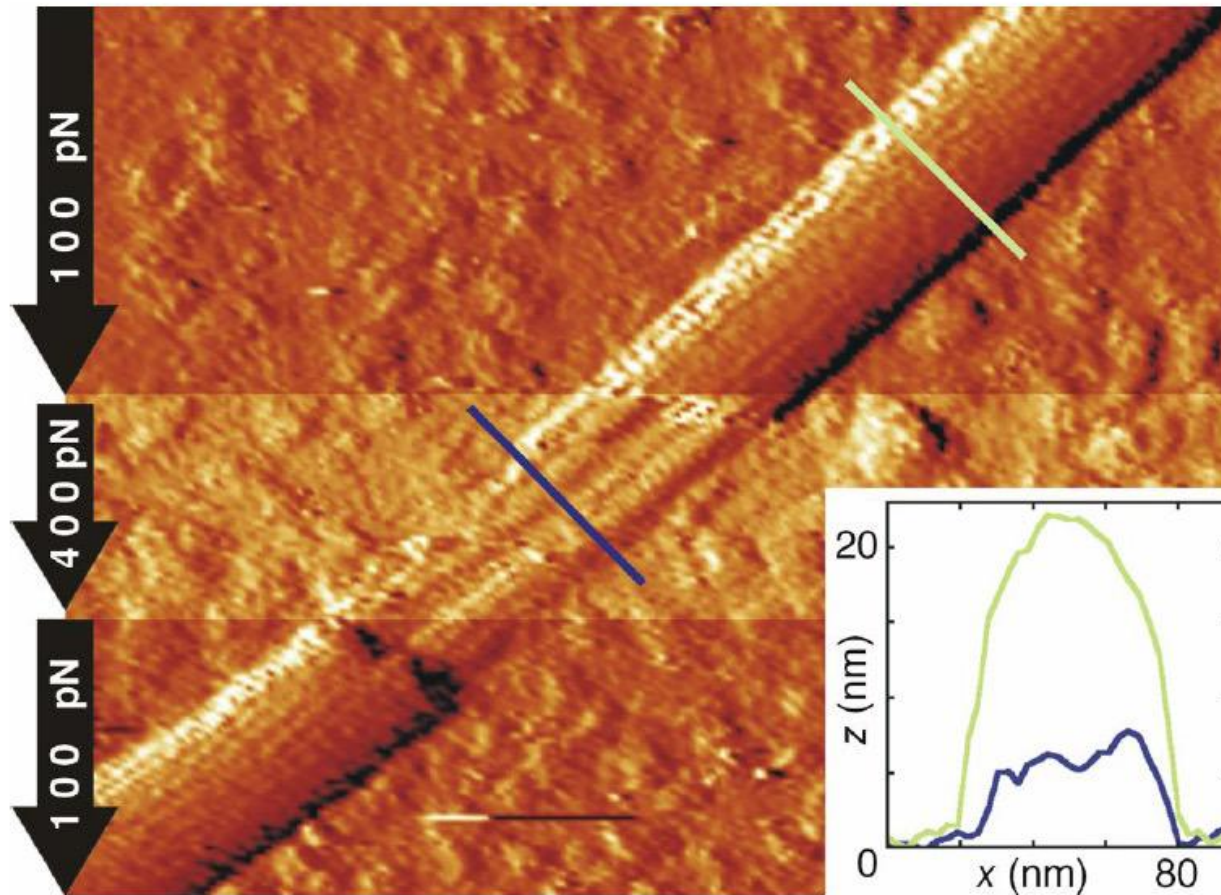
AFM in liquid
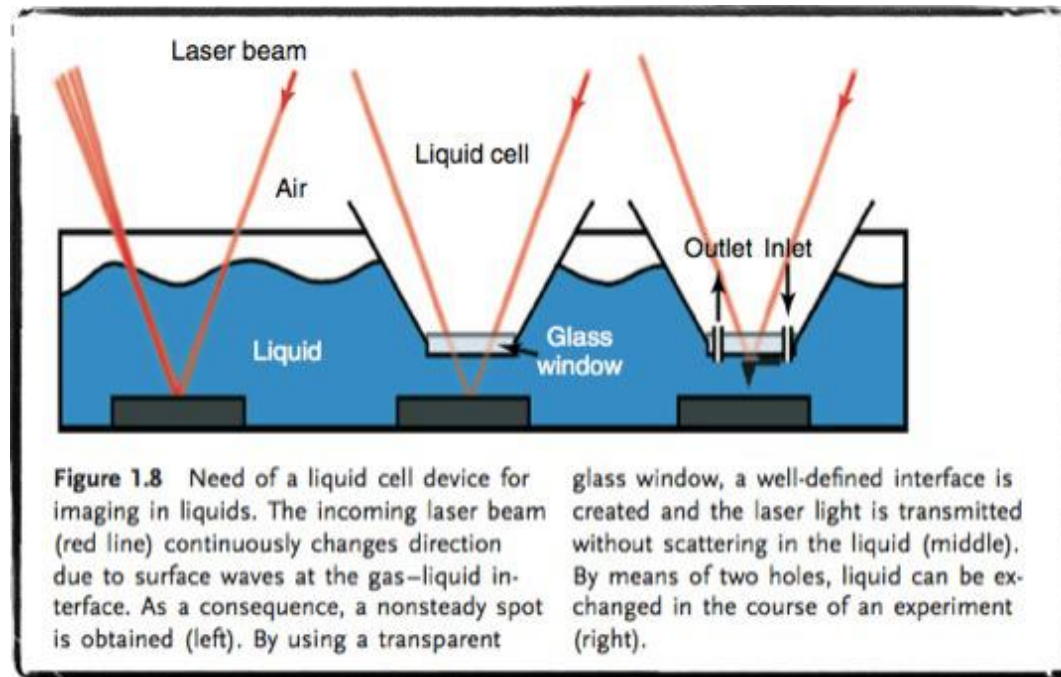
An important step of development, enabling biological AFM, was the development of a liquid cell in which cantilever, tip and sample are immersed in buffer solution.

Figure 1.8 Need of a liquid cell device for imaging in liquids. The incoming laser beam (red line) continuously changes direction due to surface waves at the gas–liquid interface. As a consequence, a nonsteady spot is obtained (left). By using a transparent glass window, a well-defined interface is created and the laser light is transmitted without scattering in the liquid (middle). By means of two holes, liquid can be exchanged in the course of an experiment (right).

Figure 1.12 Side view of a design of a liquid cell showing a possible mechanism to oscillate the cantilever. A piezoelectric ceramic is located below one of the supporting balls and far away from the liquid meniscus. This solution also moves the liquid, and that excites many other resonances of the liquid cell.

In the case of soft biological samples, non-destructive imaging at nanometer-resolution in physiological conditions (i.e. in aqueous buffer, at ambient temperature and pressure) requires the ability to control **forces < 100 pN.**
With a high optical lever sensitivity, one is able to control normal forces applied by the cantilever down to about 50 pN in liquid, enabling **contact mode imaging of biological samples.** Although lateral scanning forces impose a restriction on the sample type to be imaged in contact mode, it has yielded fascinating insights into the organization of proteins in biological membranes

sample deformation

100 pN

400 pN

100 pN

too high force destroys fragile samples

Schaap *et al*. 2004

33
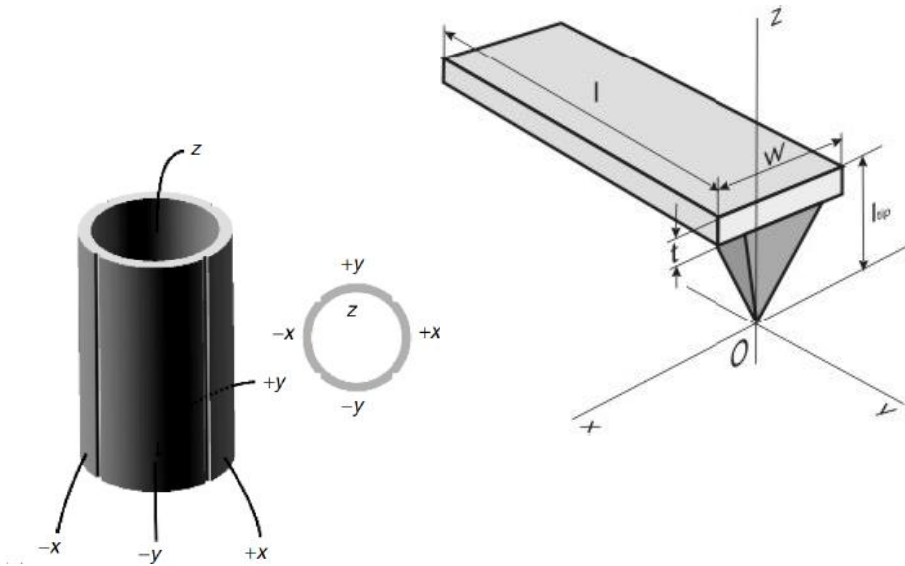
AFM in liquid

E= Young Modulus
ρ = density

$$k = \frac{E t^3 w}{4 l^3}$$

$$f = \frac{1}{2\pi}\sqrt{\frac{k}{m}} = \frac{1}{4\pi}\frac{t}{l^2}\sqrt{\frac{E}{\rho}}$$

Main concern: electrical isolation of the piezo to avoid any shortcut due to wetting
For imaging in liquids: recommended to move the tip relative to the sample to minimize the added effective mass m^* (only the tip and parts of the tip holder are immersed in the buffer container)

A cantilever in thermodynamic equilibrium with the thermal bath at temperature T has a thermal energy $k_B T$ that increases the elastic energy stored in the cantilever, giving a **thermal noise amplitude** A which can be **of the order of surface corrugation for $k = 0.1$ Nm^{-1} ($A = 0.2$ nm)**

Operation modes in liquid

Contact Mode

Feedback set point chosen depending on exp. Conditions. Drawbacks: drift of free cantilever deflection photodiode signal; friction

Jumping Mode

Developed to minimize shear forces. At each pixel, a force-extension curve is perfomed. Accurate control of force; lateral motion performed out of contact. Not applicable in air due to capillary forces. Drawback: bit slow
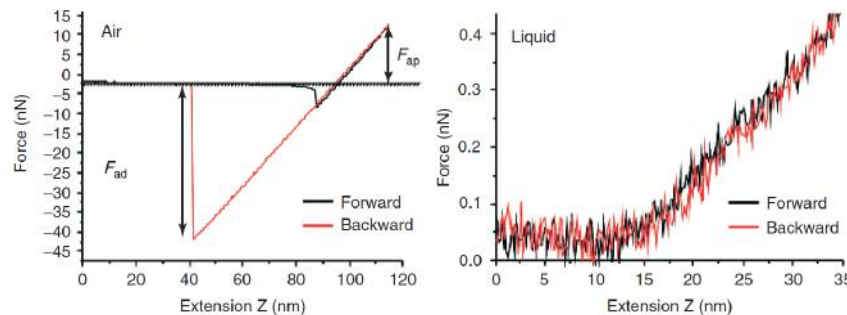

Dynamic Mode

Tapping mode: AM-AFM mode. Linear decrease of amplitude with tip-sample distance due to interaction with the surface. Reduction of amplitude in the tapping region gives the force. Comparable results, in liquid, to jumping mode, but much faster.

Jumping mode or "peak force" AFM

JM is particularly suitable for scanning in liquids, where the low adhesion forces allow using small Z displacement at each point. Because of the oscillation damping in liquid in amplitude modulation modes (NC, Tapping), JM although slow can give better performance. **N.B.: Dynamic modes use as feedback the oscillation amplitude. JM the cantilever deflection! Like in contact mode...easier. Is like a CM with the fine tuning of the zero interaction force**
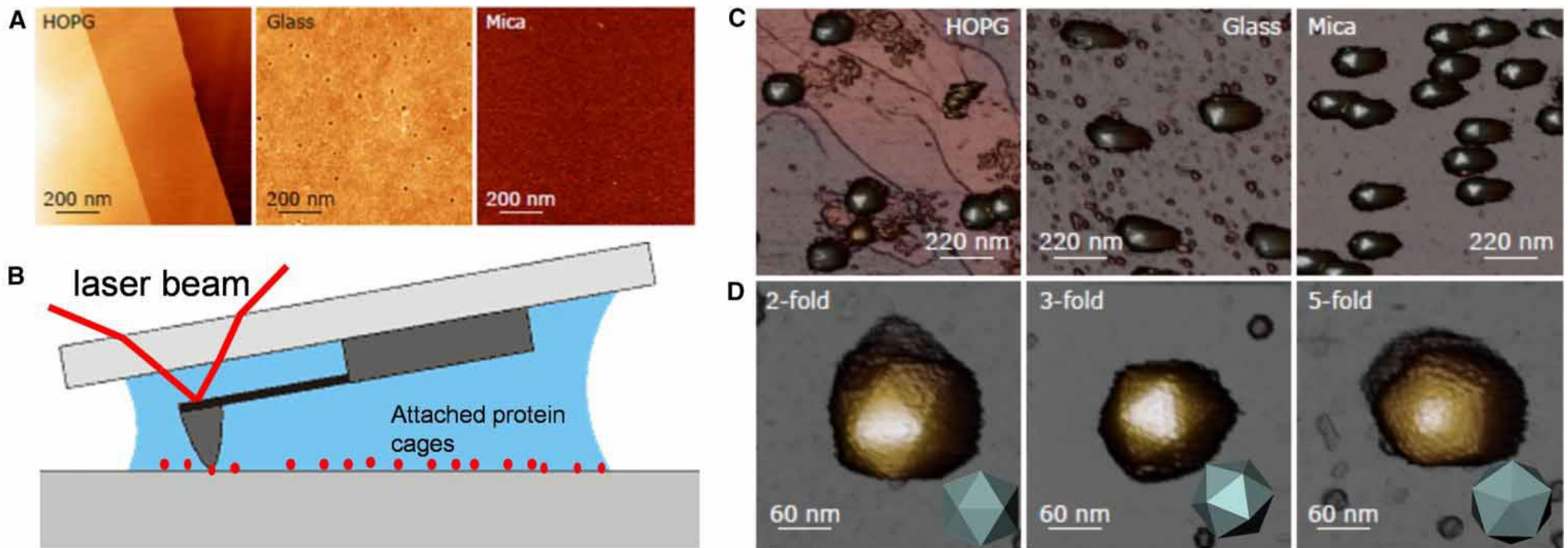

Figure 1. Attaching protein shells on surfaces.
(A) HOPG, glass, and mica bare substrates before attaching the samples. (B) Cartoon of the experimental system. Protein cages and cantilever are not in scale. (C) HAdv on HOPG, glass, and mica. (D) Individual HAdv particles showing 2-fold, 3-fold, and 5-fold symmetry axis orientations after adsorption on the surface.   HAdV has a 95 nm diameter icosahedral, non enveloped capsid enclosing a ds DNA genome

Imaging of single virus particles on different surfaces
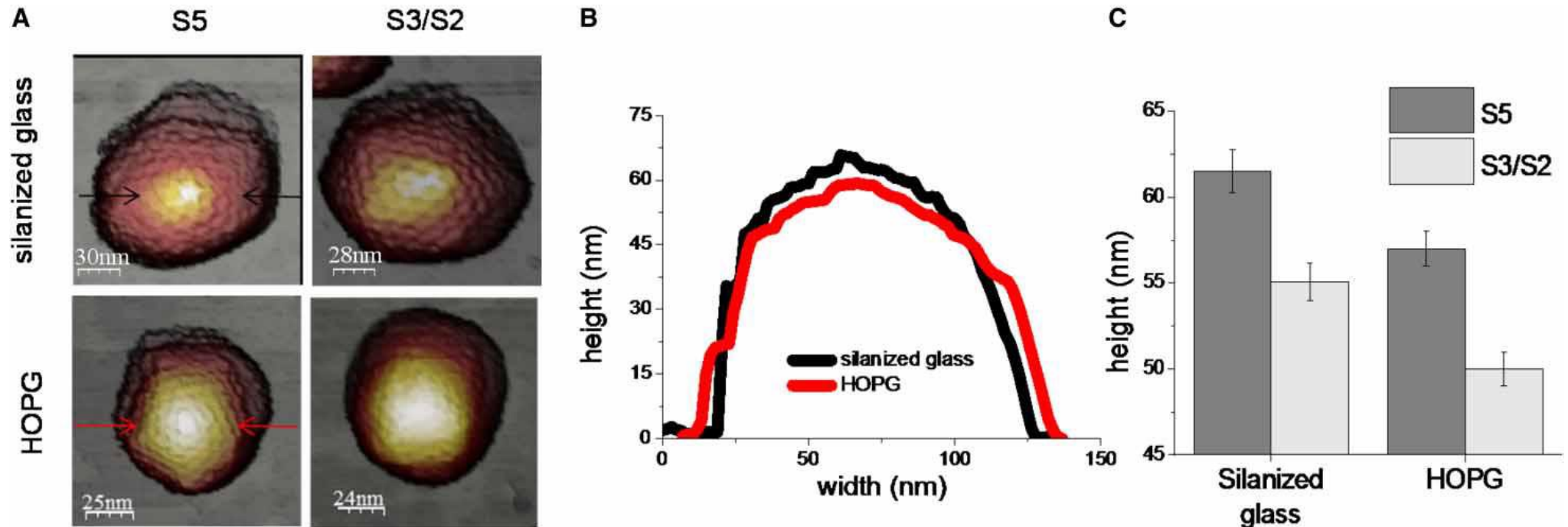
Figure 2. Protein shells collapse on the surface.

(A) P22 bacteriophage particles on glass and HOPG oriented to 5-fold and 3-/2- fold symmetry axes. (B) Comparison of topographical profiles obtained on two particles adsorbed on glass (black) and HOPG (red) obtained from **A**. (C) Comparison of average height of particles adsorbed at different orientations and substrates.

Jumping mode AFM
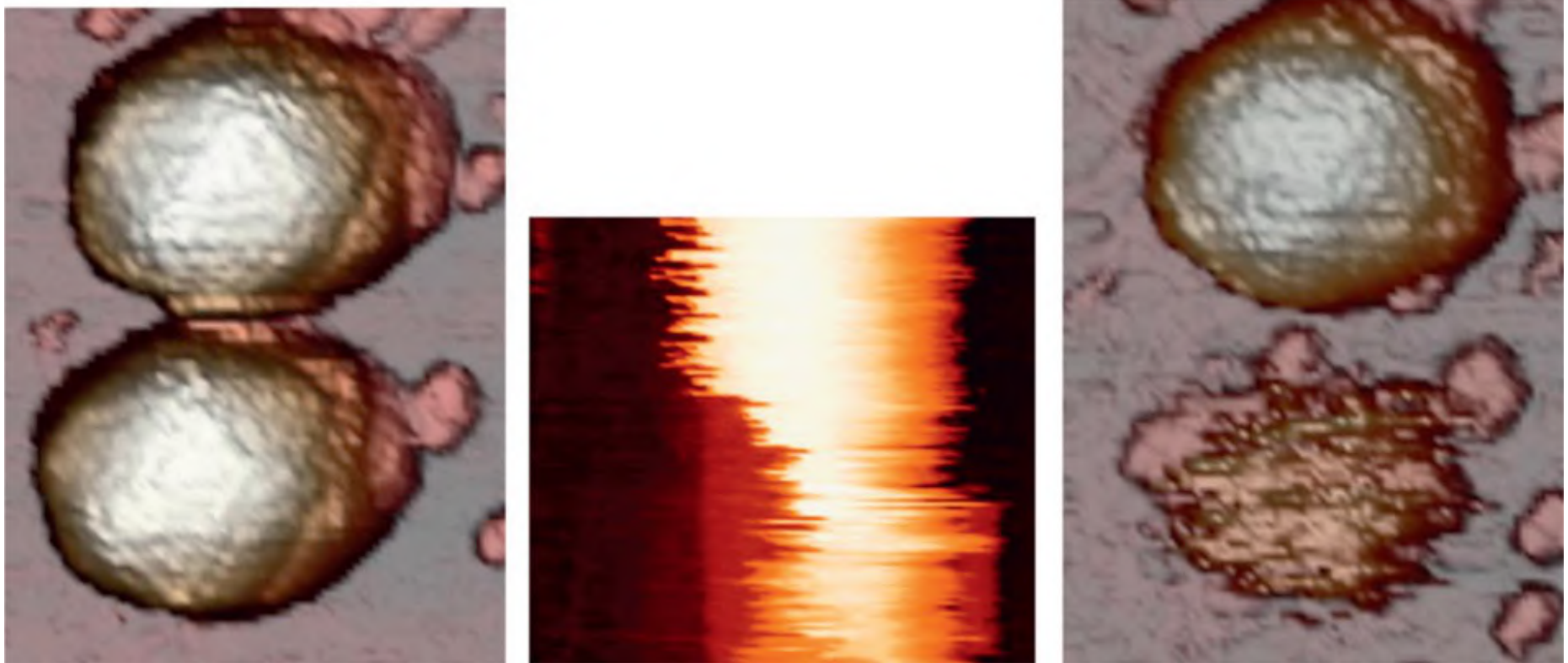
Fig. 4. (a) 250 nm × 330 nm AFM topography image of two HAdV particles acquired with JM+. (b) Time evolution (downwards) of the topography at the dashed line of figure (a). At the horizontal solid line the new algorithm is switched off, reverting to conventional JM. Notice the sudden change in the scanning profile. (c) Subsequent imaging of the same area with JM+ procedure demonstrates total destruction of the scanned virus while the other particle remains unmodified. Set point 150 pN.

under the new JM procedure, HAdV particles can be scanned for a long time without significant damage.

Figure 5. Dilation effects in the protein shell of bacteriophage P22.
(A) The EM-1826 model of P22 bacteriophage oriented to the 2-fold symmetry axis. (B) Dilated data of (A) obtained with a tip of 10 nm in diameter by using the dilation algorithm of the WSxM software. (C) AFM image of a single P22 bacteriophage oriented to the 2-fold symmetry axis. The cartoon of (D) indicates the dilation as a function of the tip size: black, red, and blue curves are the topographical profiles obtained with tips of 0.5, 10, and 15 nm in diameter, respectively.
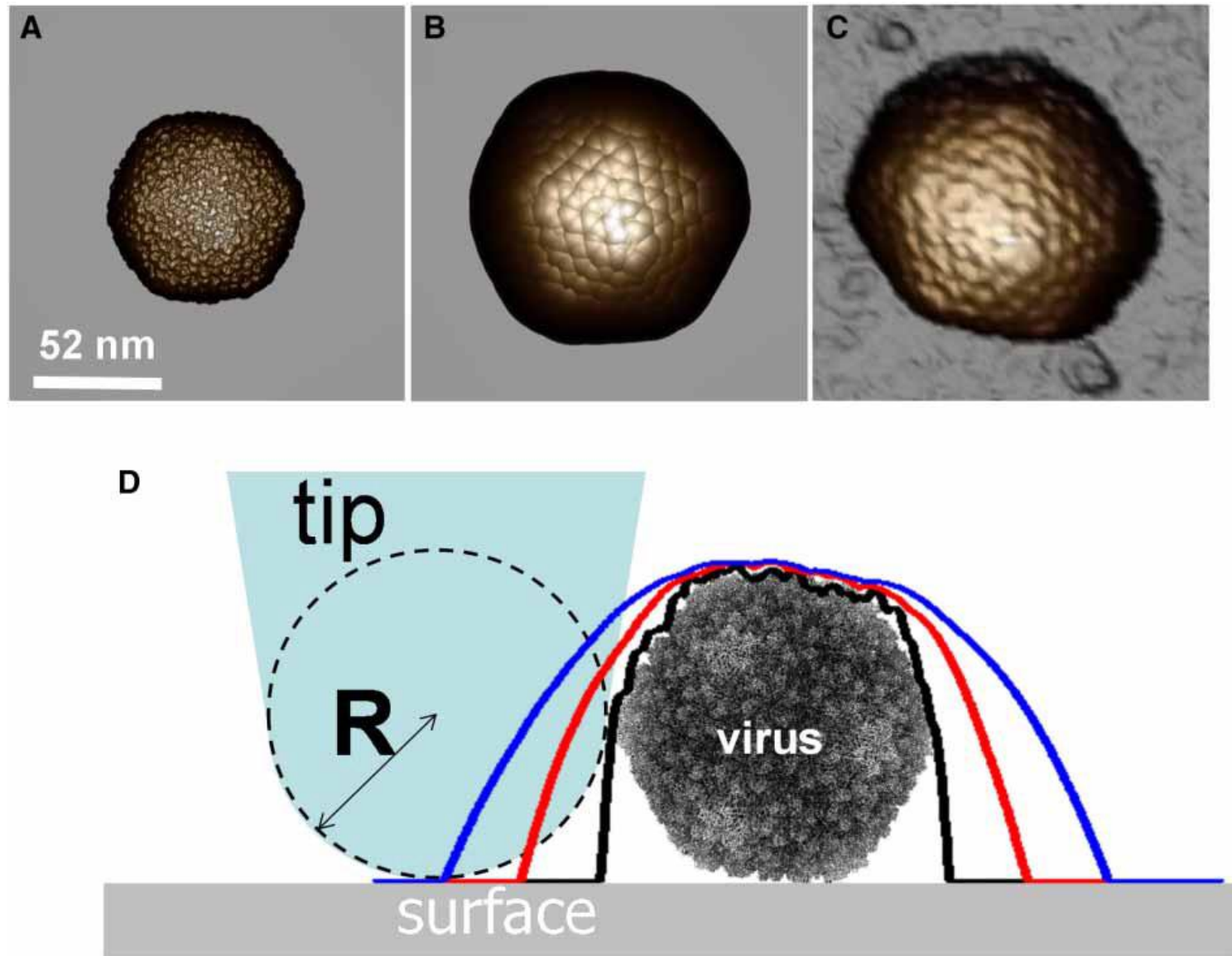
Balancing Electrostatic Forces

Main Forces in Liquid:

1) Van der Waals, globally attractive, short range.

2) Double layer forces: Repulsive, long range, dependent on pH and ionic strength. Due to ionic atmosphere over the surfaces of the tip and the surface. The 2 layers create the repulsive force.
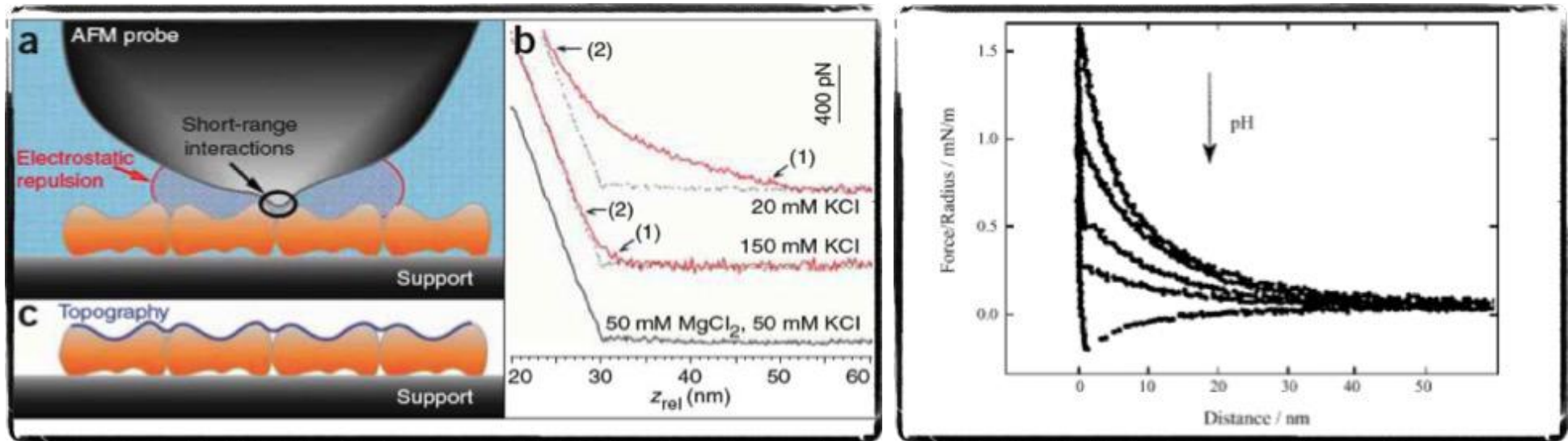
Fine tuning of electrolyte concentration is always required to minimize the distance of tip-sample electrostatic interactions and achieve high-resolution.
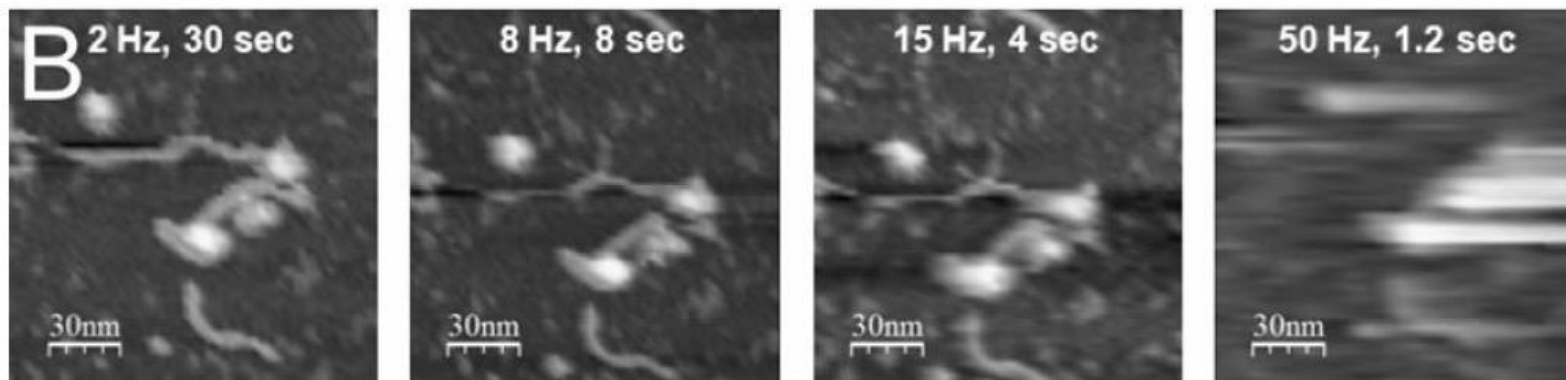
SPEED LIMITS OF AFM IMAGING
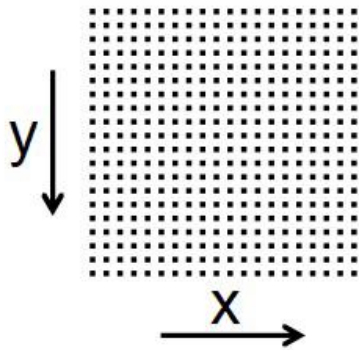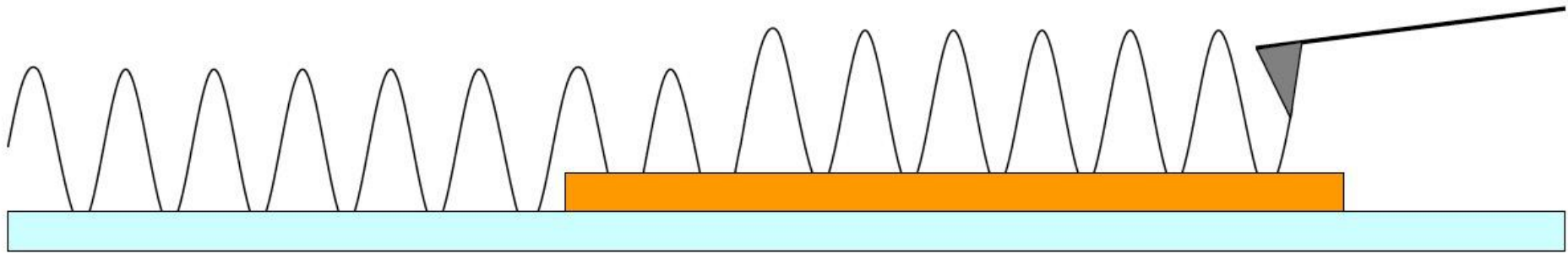
64 x 64 = 4096 px

need a few oscillations per pixel (~5)

fast bio-cantilever ~ 25 kHz

$\rightarrow$ 0.04 ms * 5 * 4096 = 1 s

B 2 Hz, 30 sec | 8 Hz, 8 sec | 15 Hz, 4 sec | 50 Hz, 1.2 sec

30nm

(there are other limiting factors (z-piezo, feed-back loop))

Courtesy of I. Schaap

SPEED LIMITS OF AFM IMAGING

64 x 64 = 4096 px

need a few oscillations per pixel (~5)

fast bio-cantilever ~ 25 kHz

$\rightarrow$ 0.04 ms * 5 * 4096 = 1 s

| B 2 Hz, 30 sec | 8 Hz, 8 sec | 15 Hz, 4 sec | 50 Hz, 1.2 sec |

30nm | 30nm | 30nm | 30nm
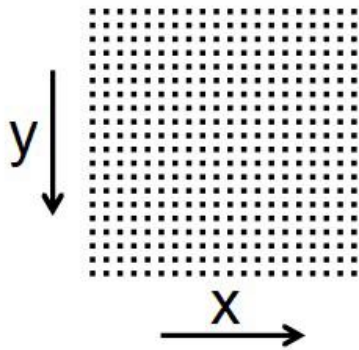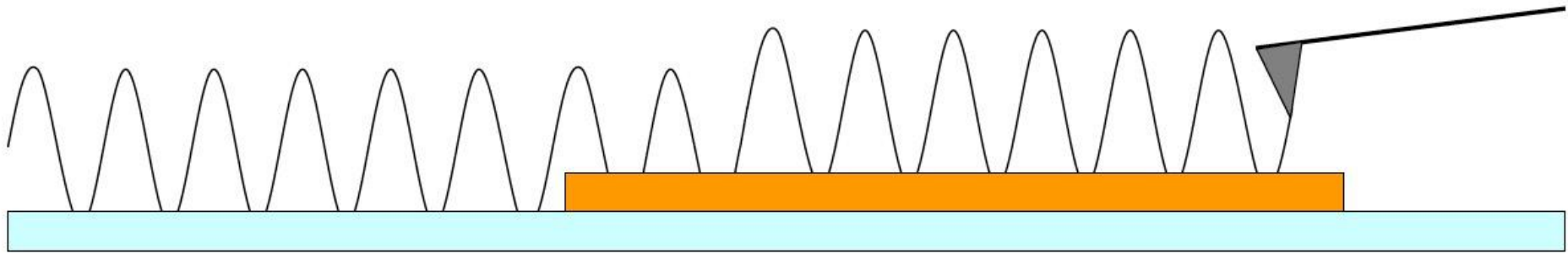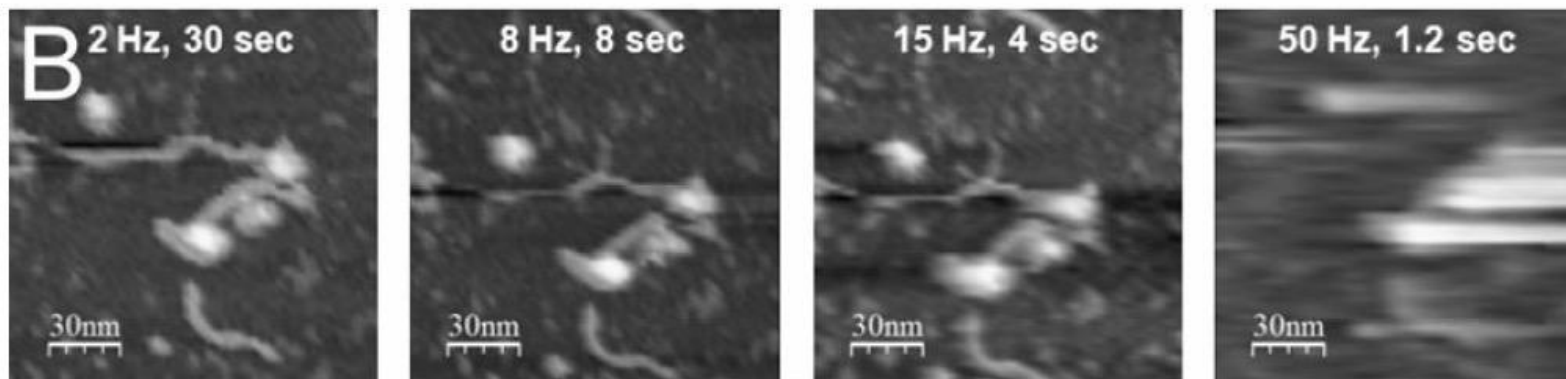
(there are other limiting factors (z-piezo, feed-back loop)

small cantilevers are faster

	l (μm)	w (μm)	t (μm)	ω_0 (kHz)	k (N/m)	
rc800	200	20	0.8	3	0.05	8 s
bl150	60	30	0.18	8	0.03	3 s
ac40	38	16	0.2	25	0.1	1 s
ac10	9	2	0.13	500	0.1	50 ms
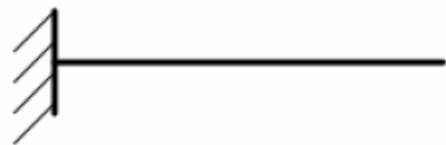
$$\omega_0 = \sqrt{k/m} = \sqrt{\frac{Et^2}{l^4 \rho}}$$

$$k = \frac{F}{d} = \frac{Ewt^3}{4l^3}$$

make cantilevers short to increase ω_0 and thinner to restore k

ATOMIC FORCE MICROSCOPY
Imaging in Biology_2
Examples

Myosine V walking on actin filaments
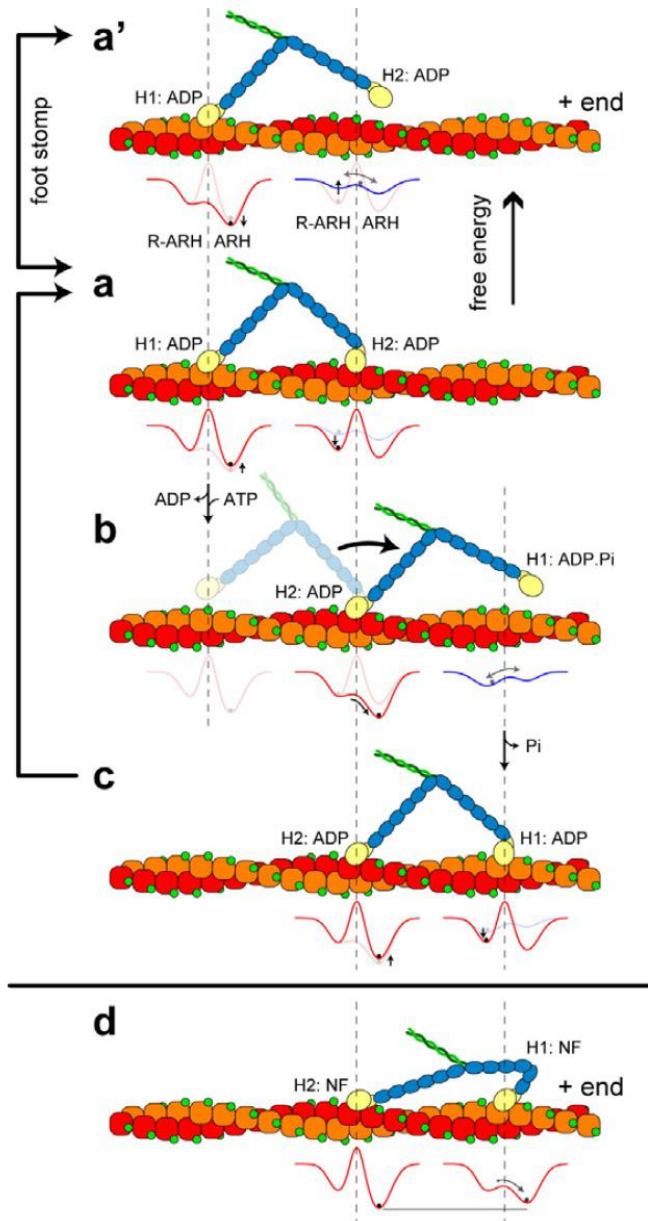
In dynamic HS-AFM the molecule itself is visualized while working and moving on its biological track, providing concomitant structural and dynamic data: not only did the observation confirm the hand-over-hand walking mechanism of myosin-V, it did reveal that the power stroke of this motor is driven by intramolecular mechanical tension

N. Kodera, D. Yamamoto, R. Ishikawa, T. Ando *Nature* **468**, 72 (2010)

Myosine V walking on actin filaments

Each head of the double-headed myosin hydrolyzes ATP into ADP and inorganic phosphate (Pi). The ATPase rate is very low when myosin is alone but is markedly accelerated by its interaction with actin, where the chemical energy liberated by ATP hydrolysis is converted into mechanical work.
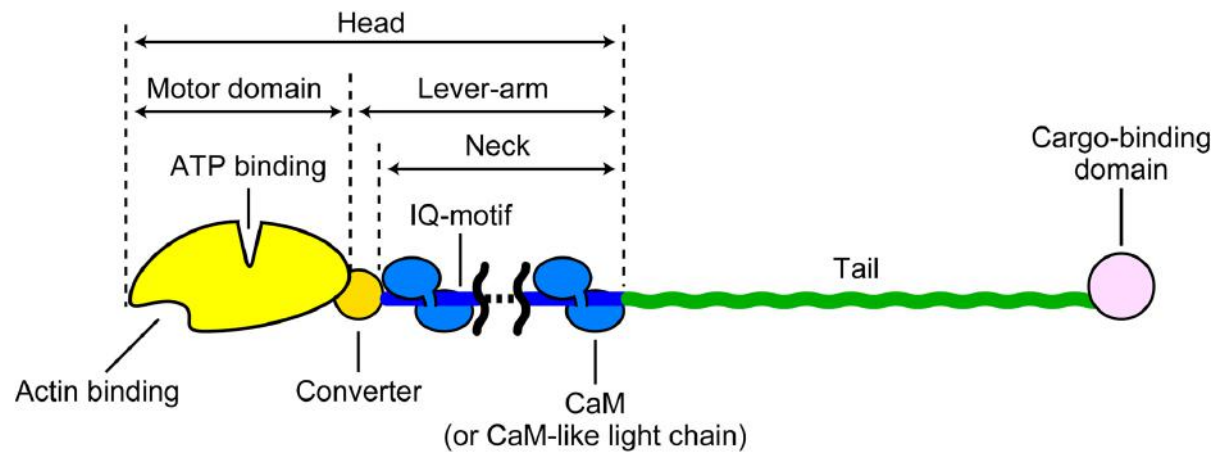
Myosine V walking on actin filaments
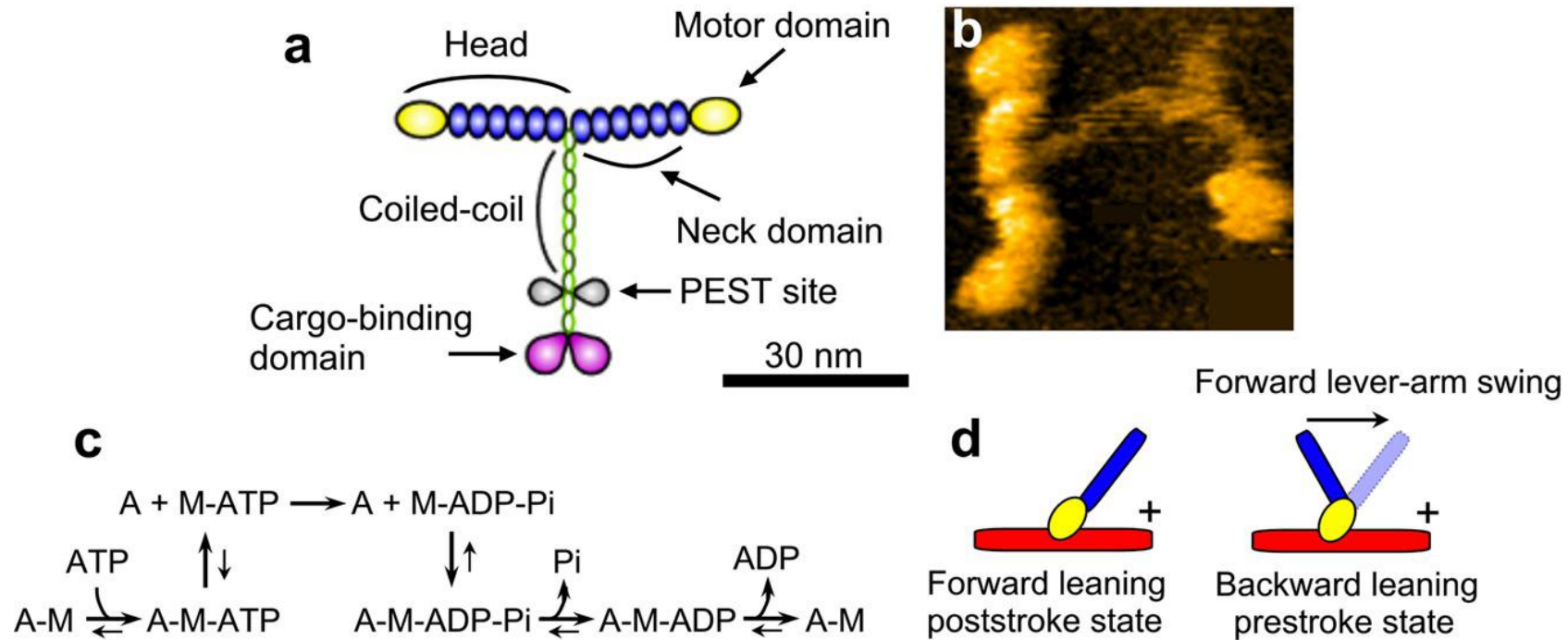
The nucleotide-free head tightly bound to actin detaches from the actin immediately after binding to ATP, quickly followed by hydrolysis of the bound ATP to ADP−Pi. When the ADP−Pi bound head is attached to actin, the bound Pi dissociates from the head, which is followed by the formation of a strongly bound tertiary complex A−M−ADP (A and M denote actin and myosin, respectively) and then by ADP dissociation, completing one ATPase cycle.

The main role of actin in the ATPase reaction is to accelerate the otherwise very slow Pi and ADP dissociation from a myosin head.

Energy in the cell: ATP

In the cell reactions that require energy are associated with ATP hydrolysis (hydrolysis= breaking down). ATP hydrolysis is an exothermic reaction, and the energy generated can be used to drive a non-spontaneous reaction.

Adenosine Tri/Di/Mono phosphate

$ATP \mapsto ADP + P$
$(\Delta H = -30$ kJ/mol$)$

$ATP \mapsto AMP + PP_i$
$(\Delta H = -30$ kJ/mol$)$
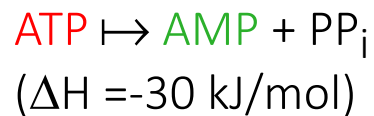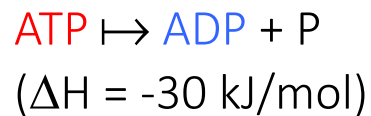
phosphodiester bonds have a large energy of hydrolysis (about 30 kJ/mol)
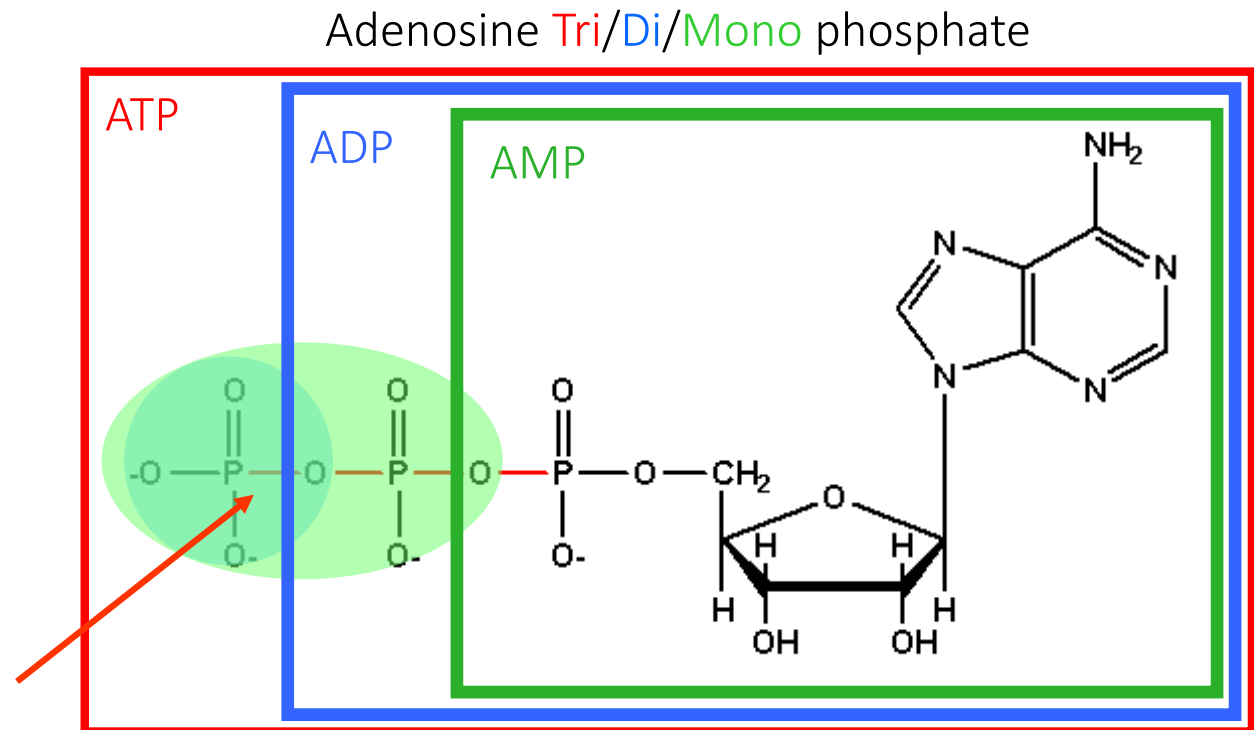
Energy production: accumulation of ATP

Energy consumption: breaking down (hydrolysis) of ATP $\mapsto$ ADP or AMP

Myosine V walking on actin filaments
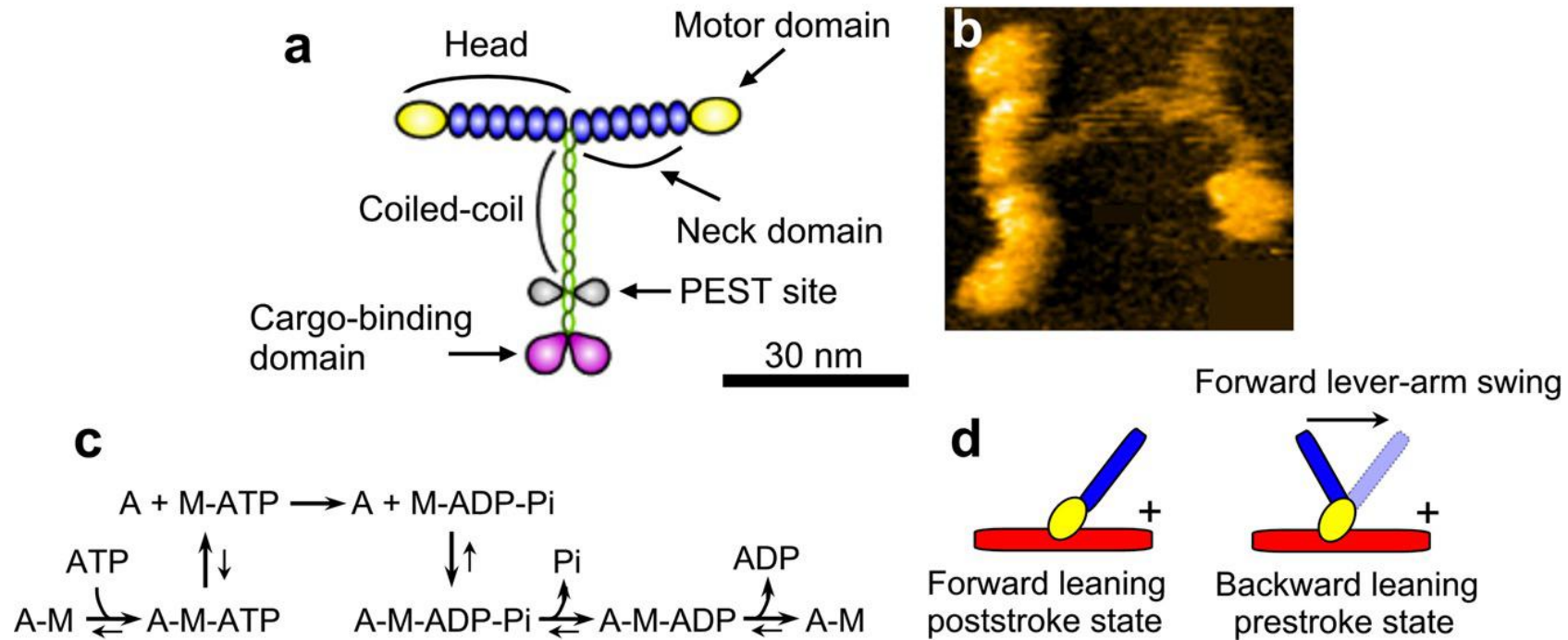
The key idea in the prevailing view on the chemo-mechanical coupling in myosin motility, which has been mainly derived from muscle myosin studies, is that the myosin head is supposed to take two different conformations, prestroke and poststroke conformations corresponding to different angles between the motor domain and the neck domain (often called "lever-arm"), depending on the nucleotide states

Fig. 4 Schematics showing in vitro motility assay systems for actomyosin. **a** Myosin-coated bead assay. The myosin-coated fluorescent beads are subjected to the polar arrays of actin cables naturally formed on chloroplastd of the alga *Nitella*, and movement of the beads are observed under a florescent microscope. **b** Actin filament gliding assay. Myosin molecules are attached to the surface of a nitrocellulose-coated coverslip and gliding motion of the fluorescently labeled actin filaments are observed under a fluorescence microscope
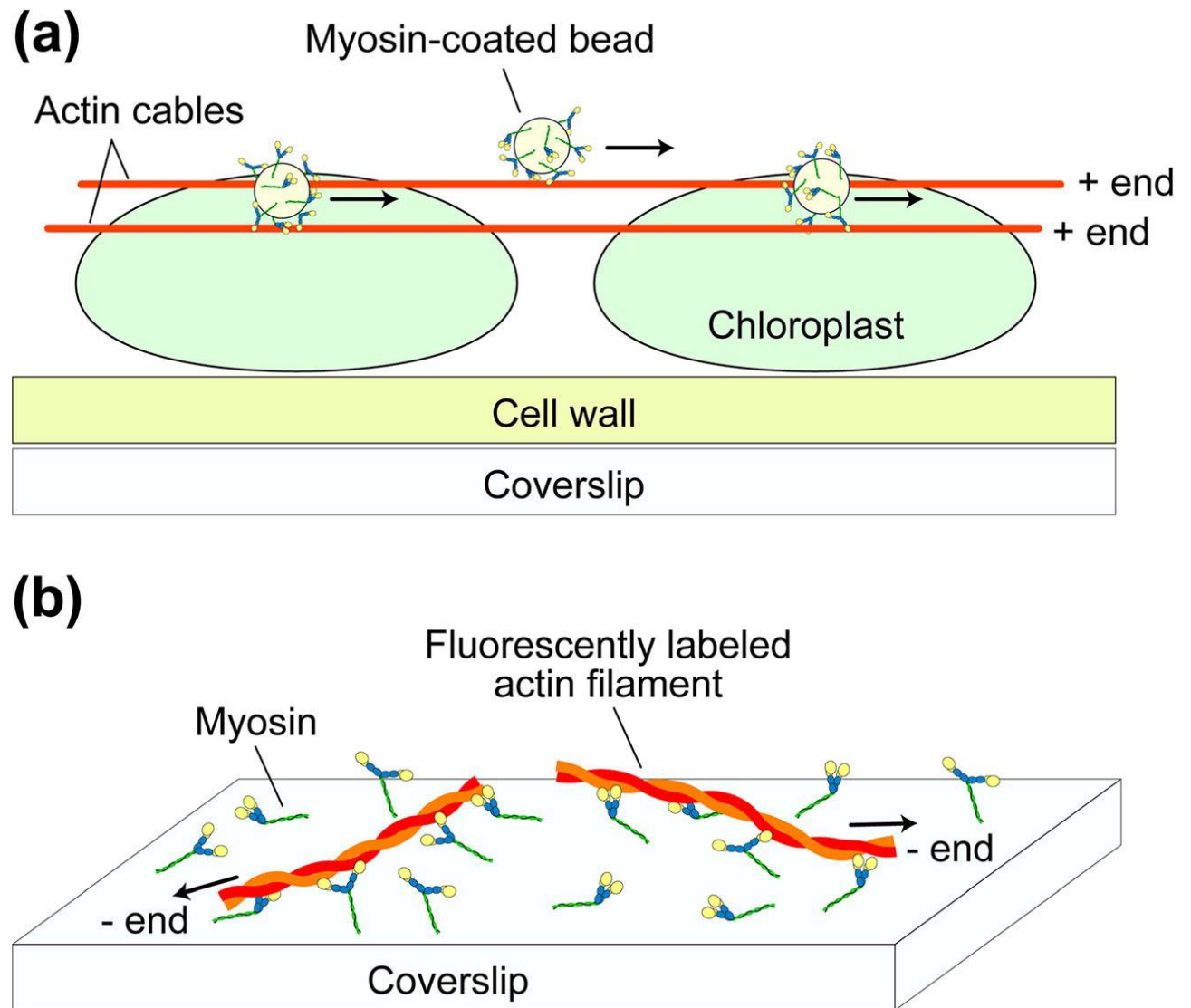
Myosine V walking on actin filaments
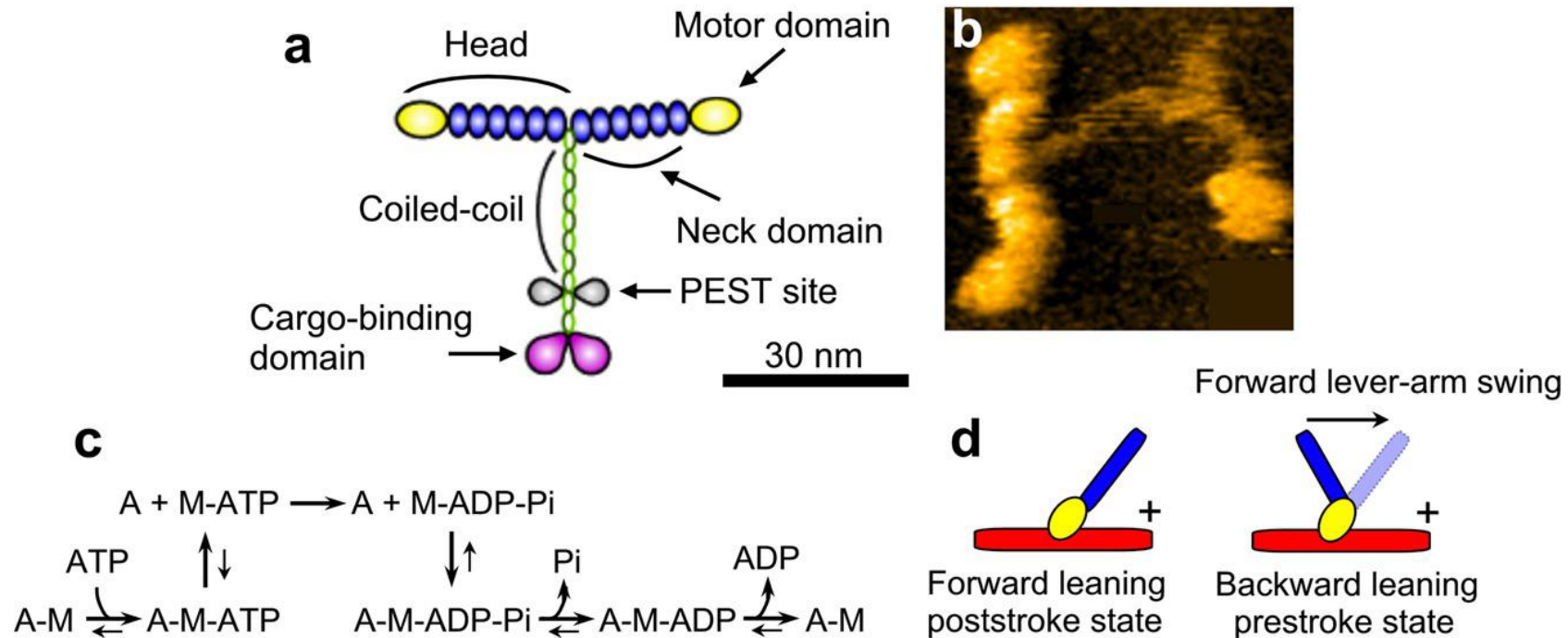
High-speed atomic force microscopy (HS-AFM), allow video-recording the structure and dynamics of functioning biomolecules at single-nanometer resolution, without disturbing their function. It helped to discover that the tension responsible for forward movement can be generated without any chemical transition, meaning that no chemical energy input is required for the tension generation. Moreover, the lever-arm swing (powerstroke) by the leading head spontaneously occurs when the trailing head detaches, thus demonstrating that no chemical energy input is required for the lever-arm swing either.

Myosine V walking on actin filaments

Video imaging by high-speed AFM has been applied to capture the dynamic behaviour of myosin V (two headed motor that functions as cargo transporter in cells) translocating along an acting filament. Moves hand-over-hand, 36 nm per ATP hydrolysis

Supplementary Figure 1 | Schematic of assay system for HS-AFM imaging (not scaled). A mica surface was fully covered with biotin-containing lipid bilayers. Streptavidin molecules (green circles) were partially deposited on the substrate. Biotinylated actin filaments were immobilised on the bilayer surface through streptavidin molecules. M5-HMM was deposited on the lipid bilayers. All imaging experiments were performed in the tapping mode using a laboratory-built high-speed AFM apparatus[5,6].

A positively charged lipid in the mixed lipid bilayer was necessary to assure weak interaction with Myosine and translocation along the actin filament

N. Kodera, D. Yamamoto, R. Ishikawa, T. Ando *Nature* **468**, 72 (2010)
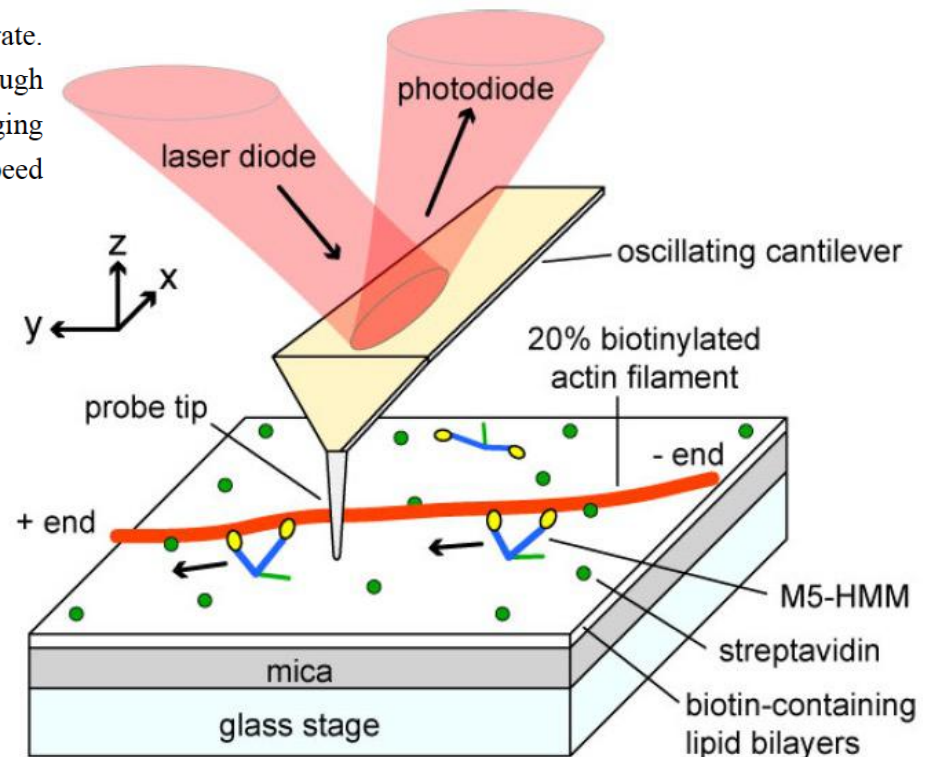
Myosine V walking on actin filaments
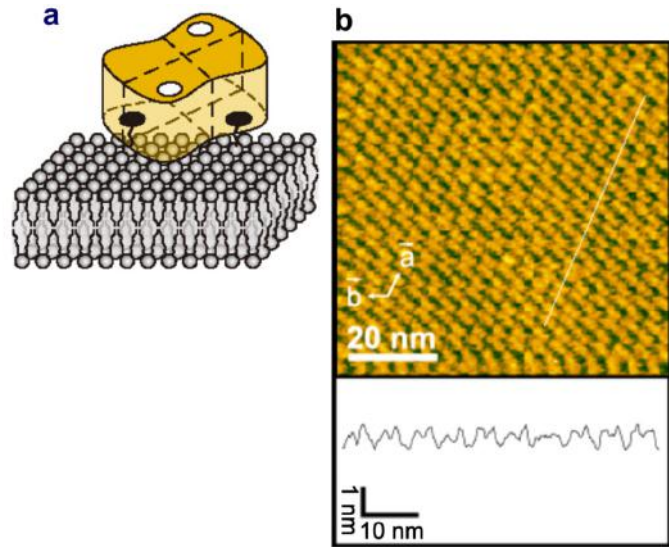
Streptavidin is a homo tetramer with dihedral D2 symmetry. Importantly, it is not favorable to nonspecific binding of many proteins, while each subunit has a high affinity biotin binding site. Streptavidin 2D crystals are easily formed onmthe surface of a fluid SLB containing biotin-lipid.

On the SLBs, two of the four biotin binding sites of streptavidin face the lipid bilayer and are occupied by biotin, whereas the other two are exposed to the aqueous environment and accessible. Therefore, biotinylated samples can be specifically immobilized on the surface of streptavidin 2D crystals
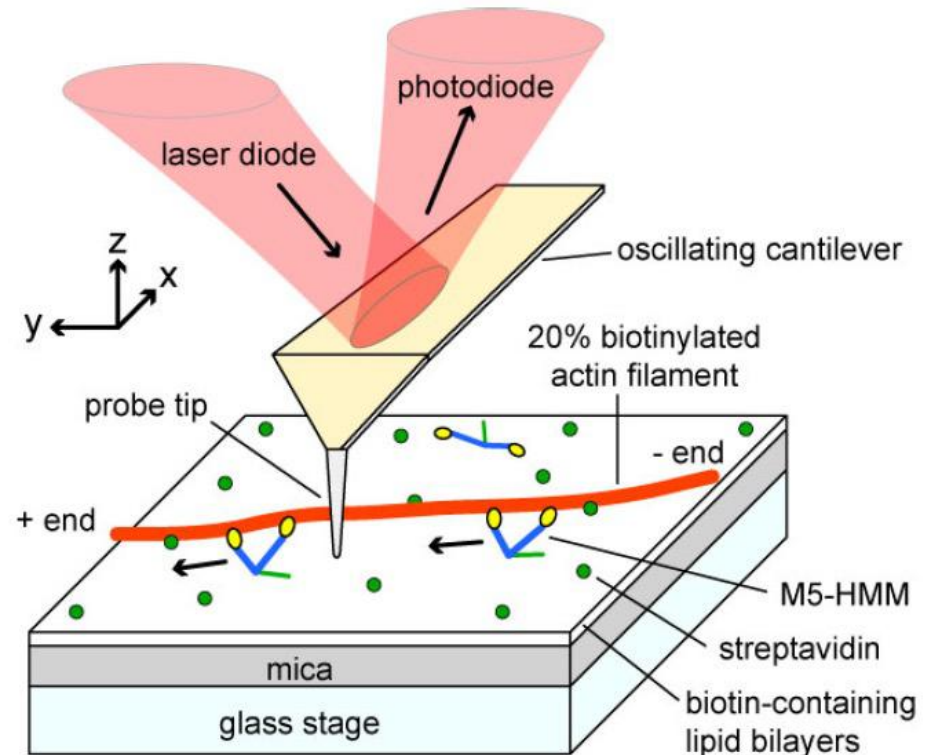
Myosine V walking on actin filaments
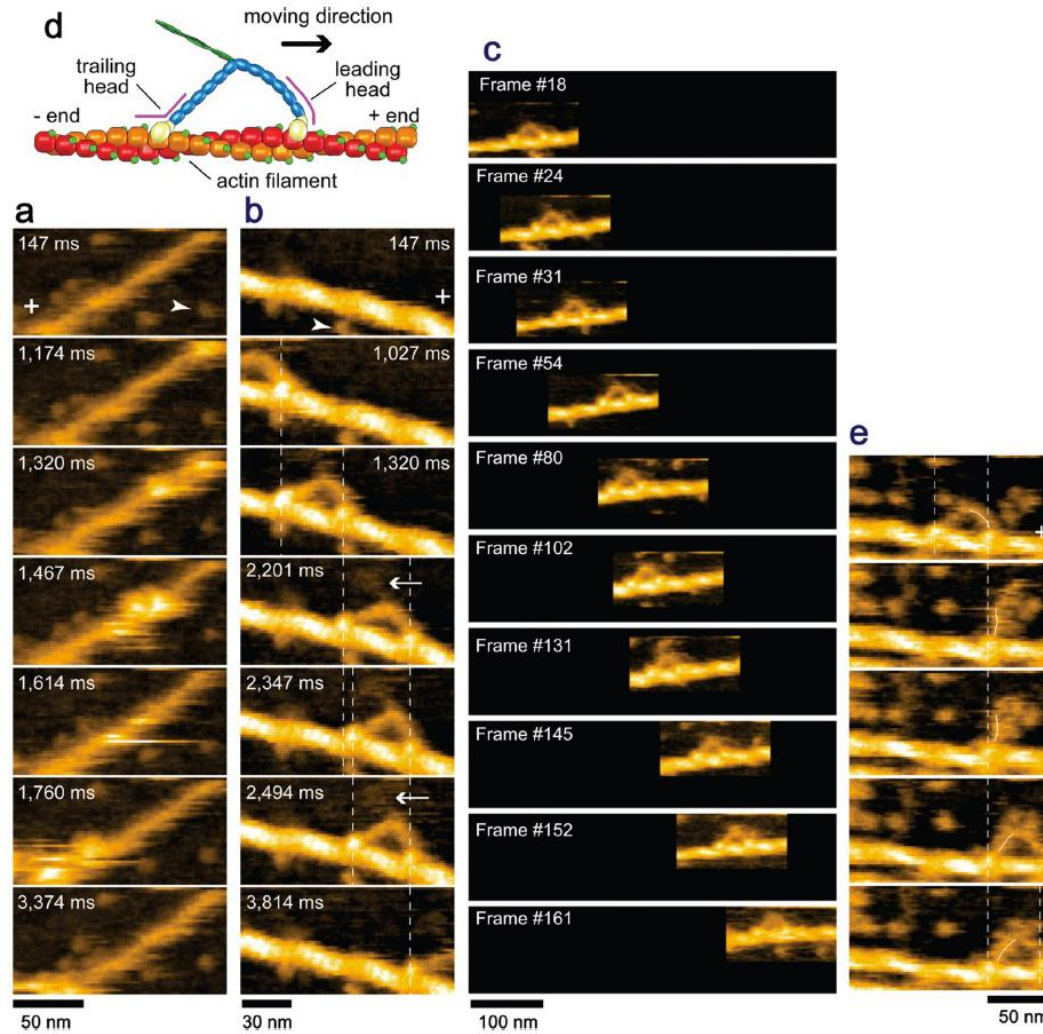
Myosine V walking on actin filaments

AFM images demonstrate a hand-over-hand movement, with swinging lever-arm motion : the detached T-head rotationally diffused around the advancing neck-neck junction. Extra STV needed as an "obstacle" to slow down the motion to be visualized (100 ms/frame)
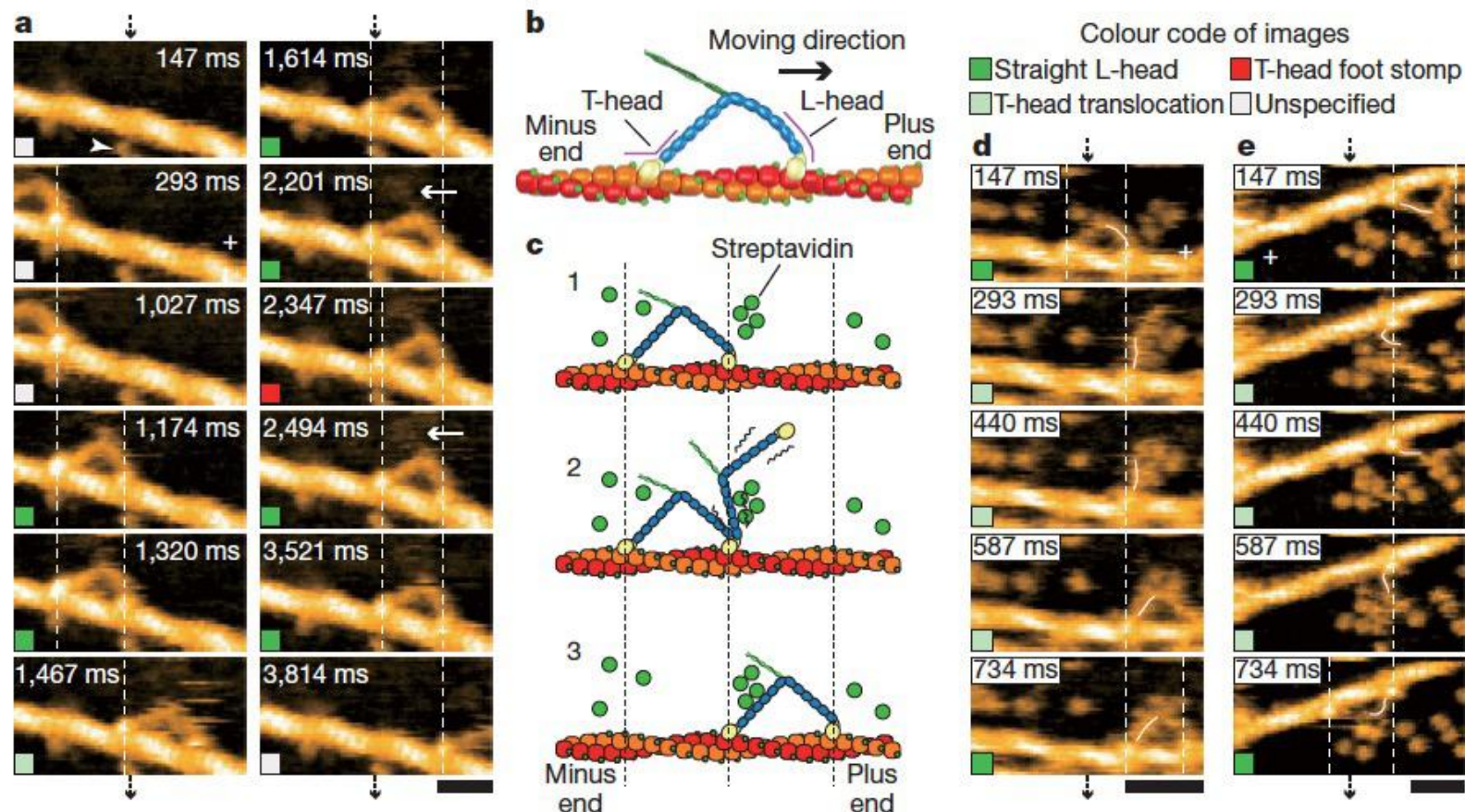
N. Kodera, D. Yamamoto, R. Ishikawa, T. Ando *Nature* **468**, 72 (2010)

http://biophys.w3.kanazawa-u.ac.jp/M5_movies.htm

Myosine V walking on actin filaments

The neck–motor domain junction appears smooth in the leading head (L-head) but is V-shaped in the trailing head (T-head) without exception.
The short coiled coil tail was mostly tilted towards the minus end of actin

N. Kodera, D. Yamamoto, R. Ishikawa, T. Ando *Nature* **468**, 72 (2010)

http://biophys.w3.kanazawa-u.ac.jp/M5_movies.htm

Myosine V walking on actin filaments

The neck–motor domain junction appears smooth in the leading head (L-head) but is V-shaped in the trailing head (T-head) without exception.
The short coiled coil tail was mostly tilted towards the minus end of actin

N. Kodera, D. Yamamoto, R. Ishikawa, T. Ando *Nature* **468**, 72 (2010)

http://biophys.w3.kanazawa-u.ac.jp/M5_movies.htm
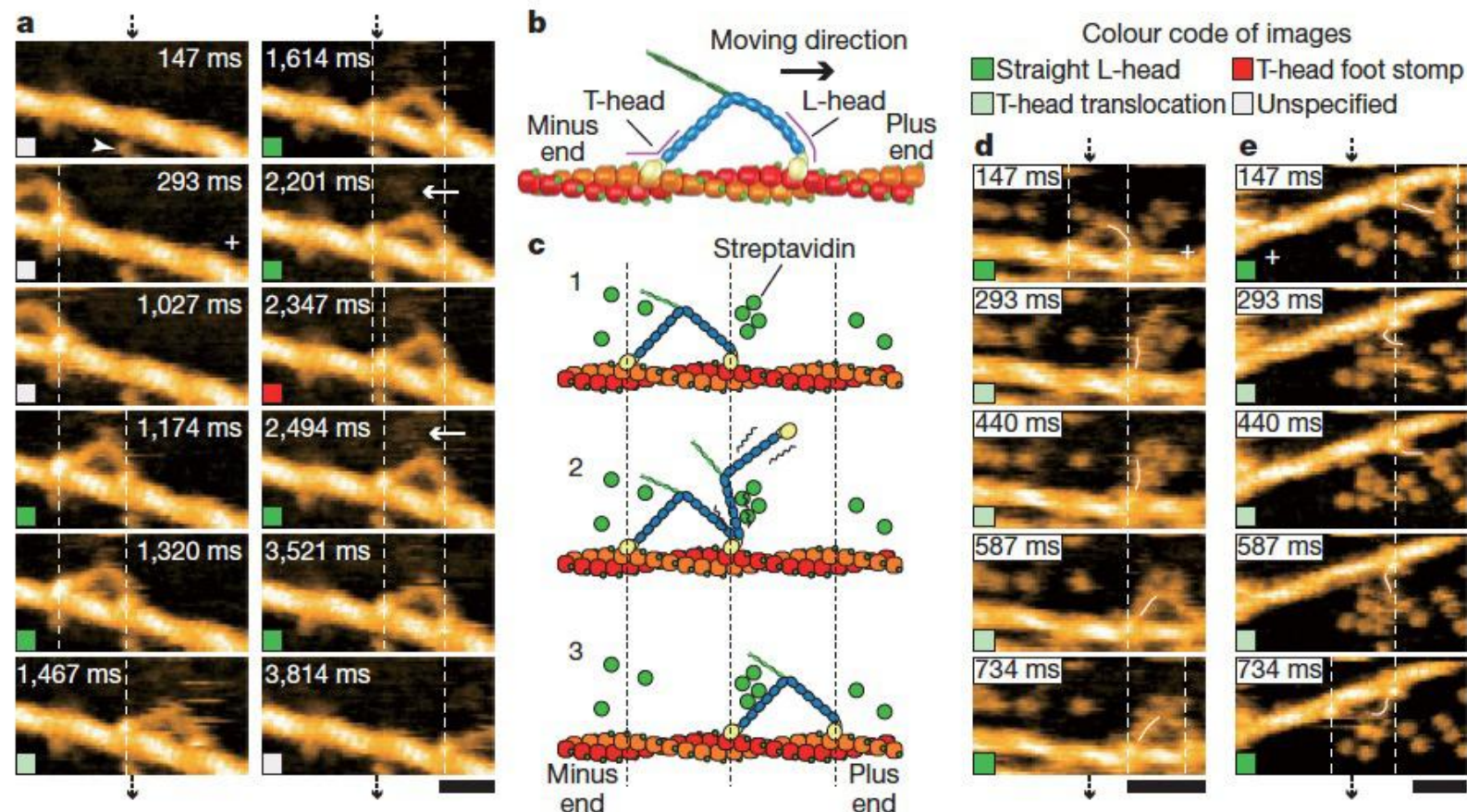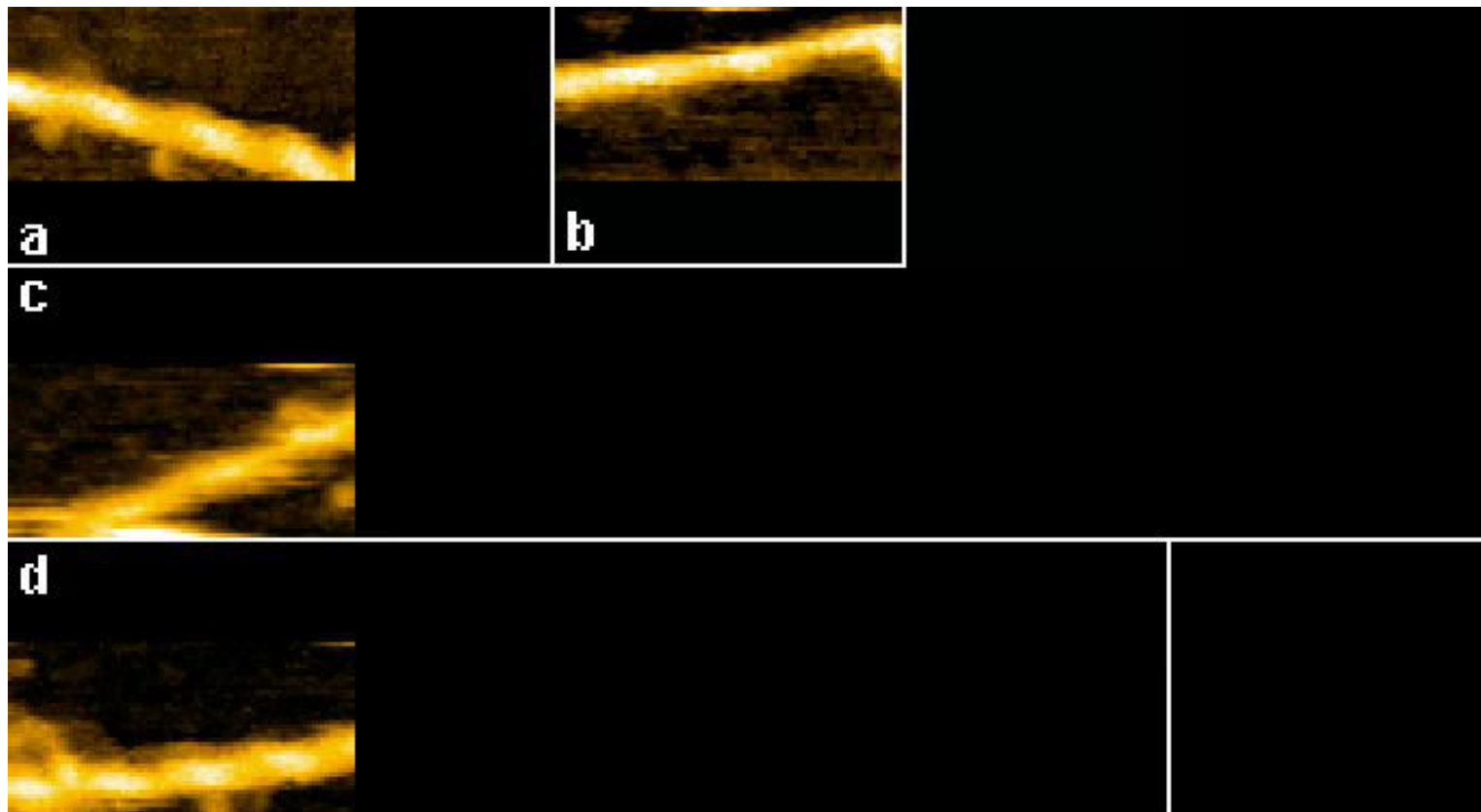
Myosine V walking on actin filaments

After T-head detachment, the nearly straight leading neck swung from the reverse arrowhead (R-ARH) orientation to the arrowhead (ARH) orientation (Supplementary Movie 2), confirming the swinging lever-arm motion initially proposed for muscle myosin. The detached T-head rotationally diffused around the advancing neck–neck junction (no translational diffusion on the actin occurs) and then bound to a forward site on the actin filament, completing one step.
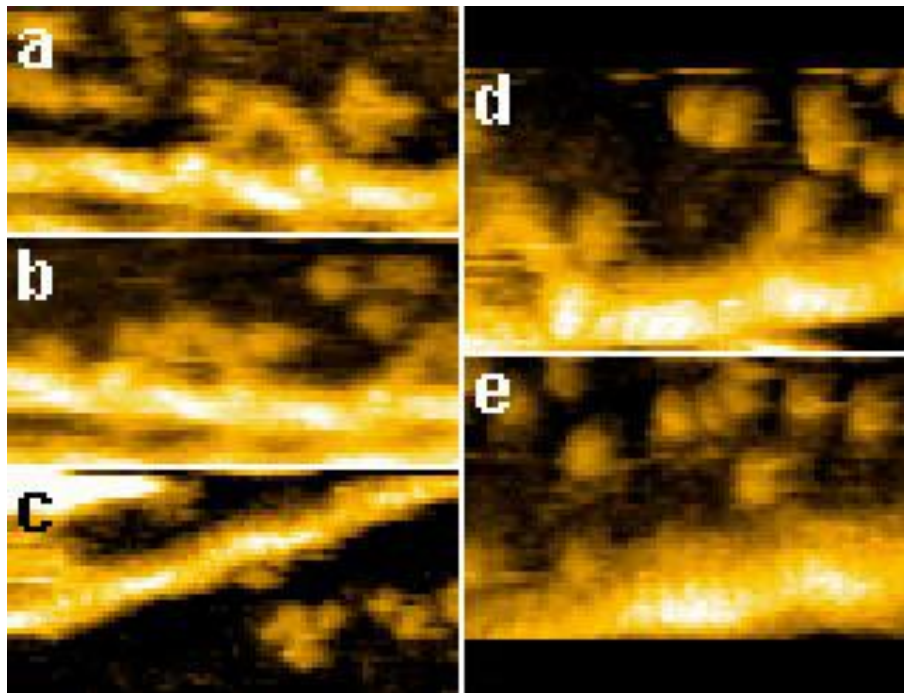
The captured images show that the forward movement is driven not by bending but by rotation of the L-head. The rotation seems to occur spontaneously after T-head detachment, suggesting that intramolecular tension driving the L-head swing exists in the two-headed bound molecules.

N. Kodera, D. Yamamoto, R. Ishikawa, T. Ando *Nature* **468**, 72 (2010)

Single molecule imaging

HR-AFM imaging: DNA

Also, high-resolution AFM imaging has been recently employed to study topological details of DNA/RNA – enzymes interaction. For example, the upstream interaction of Escherichia coli RNA polymerase (RNAP) in an open promoter complex (RPo) formed at the PR and PRM promoters of bacteriophage λ.

I. Mangiarotti, S. Cellai, W. Ross, C. Bustamante, C. Rivetti, *L. Mol. Biol.* **385**, 748 (2009)
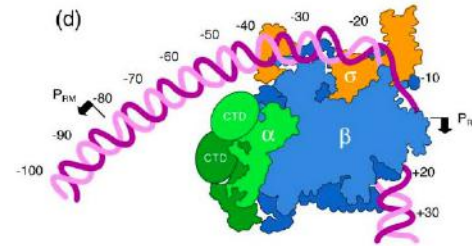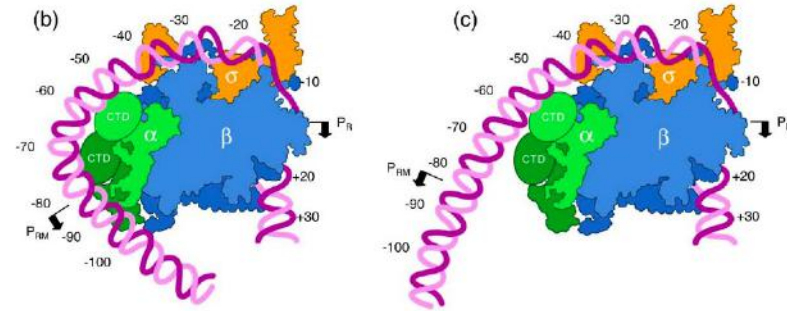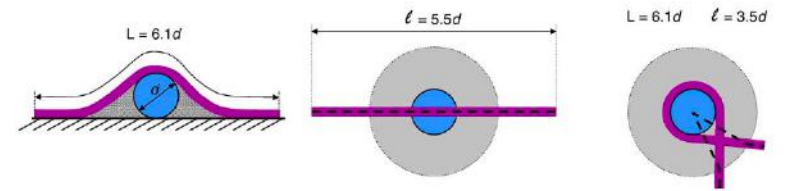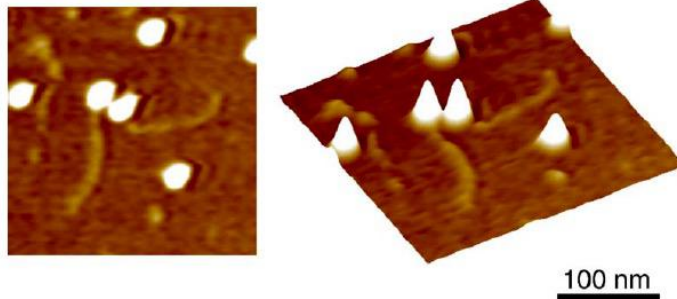
Prokaryotic transcription
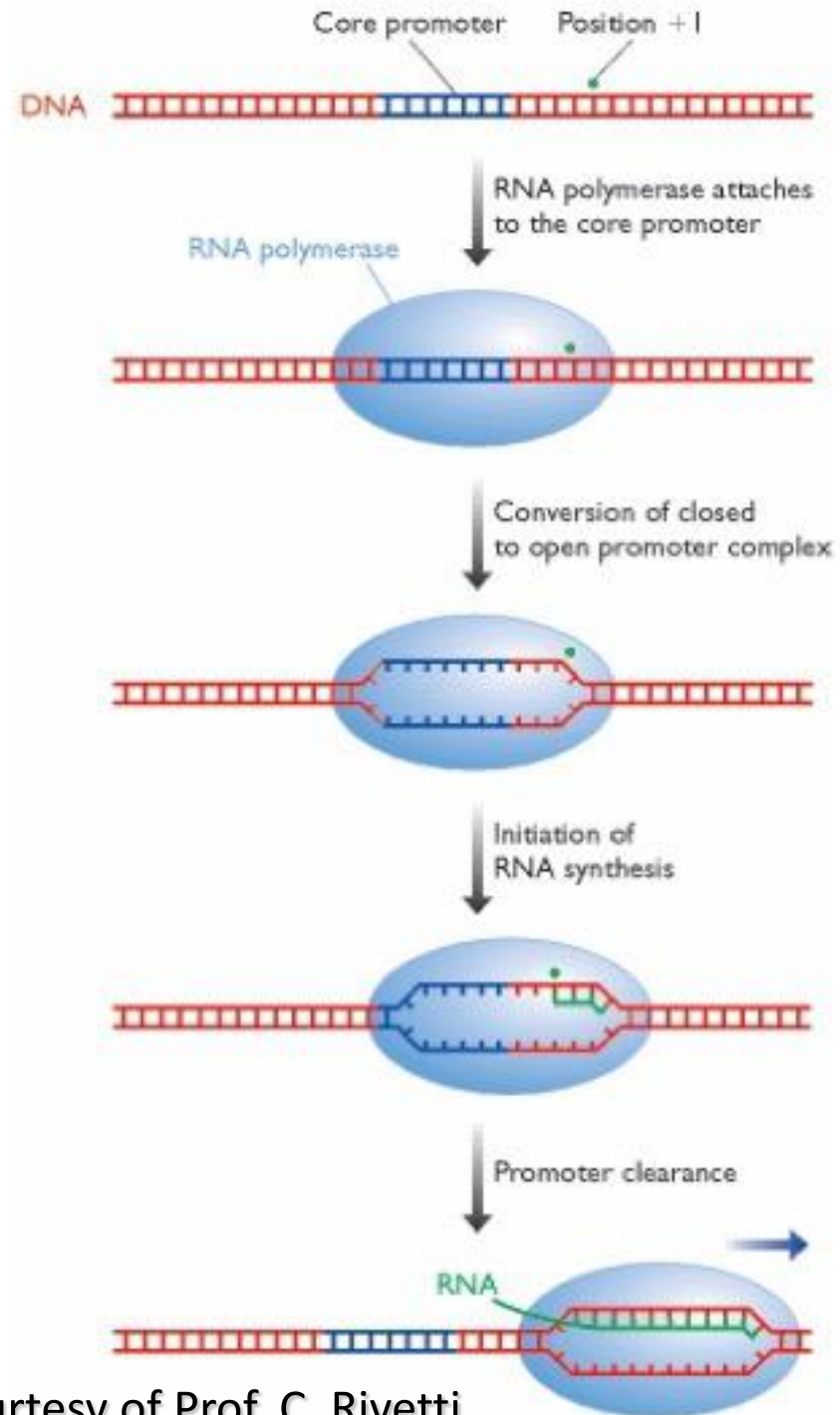
Courtesy of Prof. C. Rivetti

Struttura del DNA

Timina

Adenina

coda 5'

coda 3'

Scheletro
fosfato-
deossiribosio

coda 3'

Guanina

Citosina

coda 5'

$\varnothing$ = 2 nm

3.4 nm
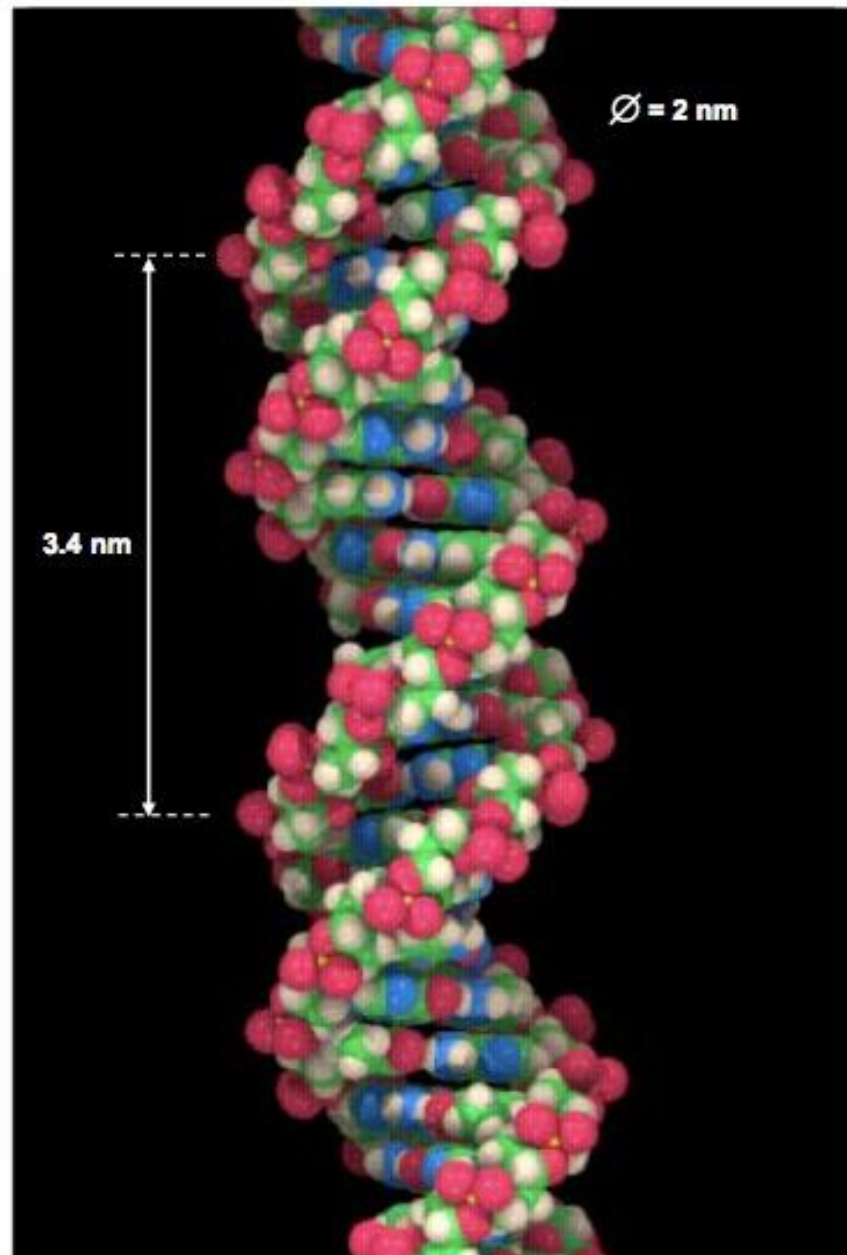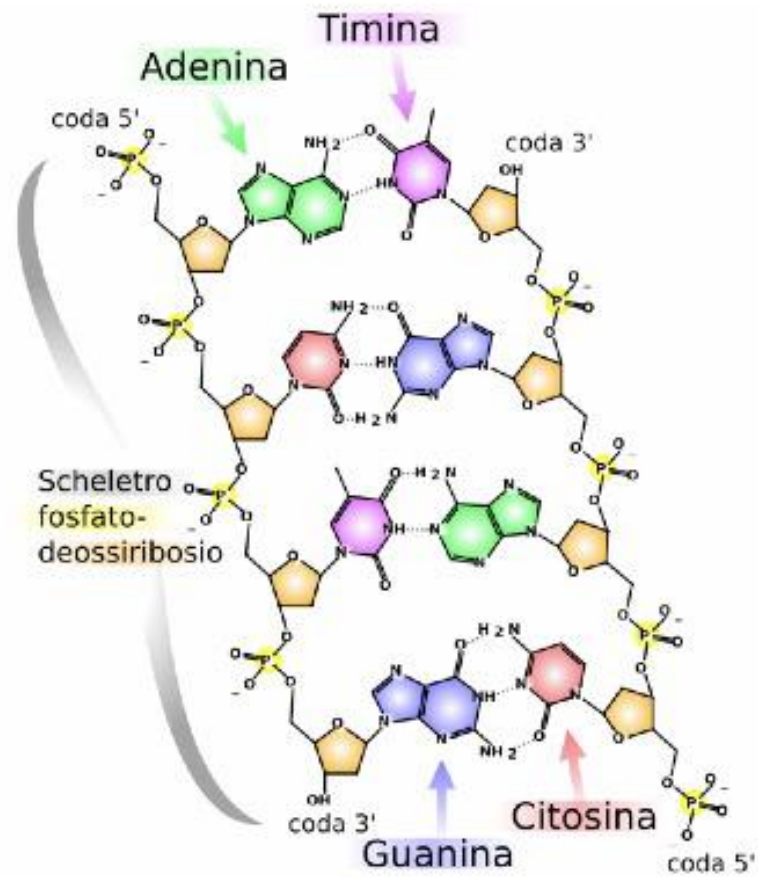
DNA

Watson and Crick, 1953

Leung et al., Nanoletters 2012

5'
3'
0.34 nm
Minor groove
3.4 nm
Major groove
3'
5'

(a) Miniaturized cantilever
20 μm
Conventional cantilever

(b)
10 μm

(c)
Amplitude [nm]
0.8
0.5
0.2
Thermal Noise [fm/√Hz]
30
20
10
1.00 1.25 1.50 1.75 2.00
Frequency [MHz]
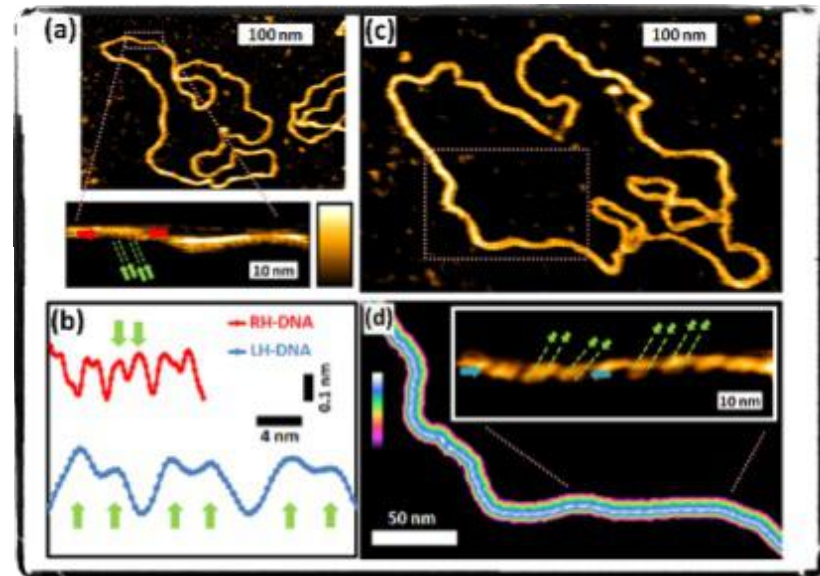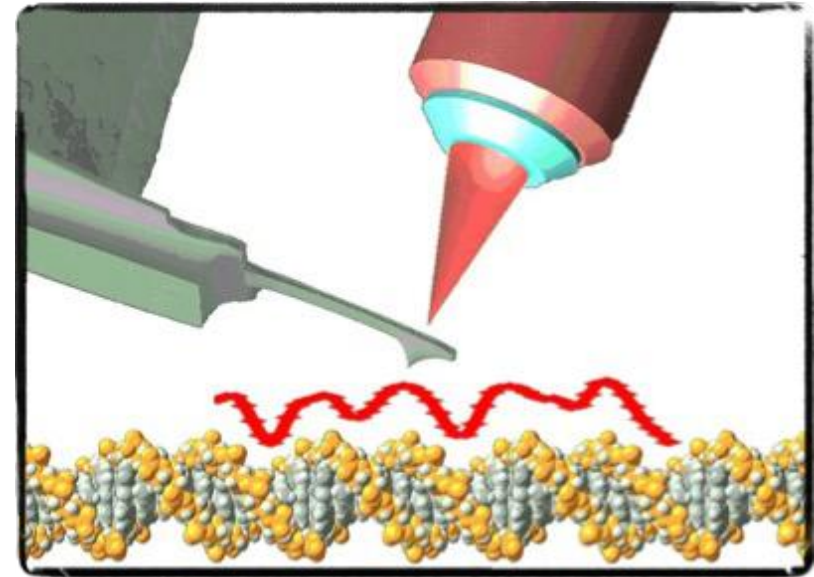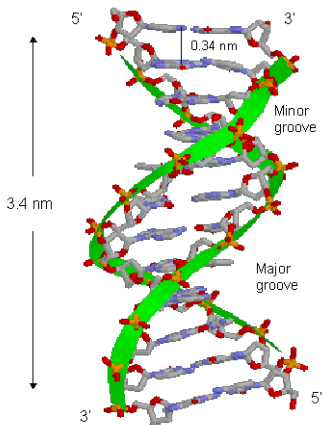
AFM image simulation of DNA

Rc = 7.0 nm   Rc = 5.0 nm   Rc = 4.0 nm   Rc = 2.0 nm

Rc = 1.0 nm   Rc = 0.5 nm   Rc = 0.1 nm
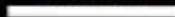
20 nm

Rc = 0.1 nm
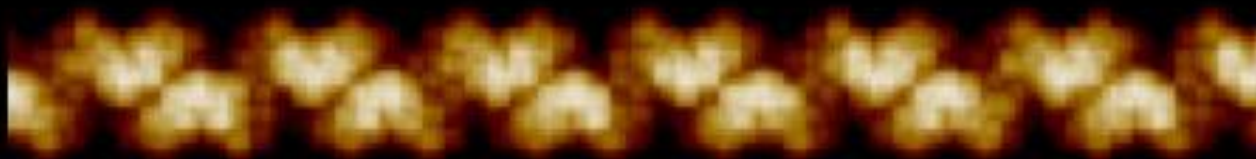
3.0 nm
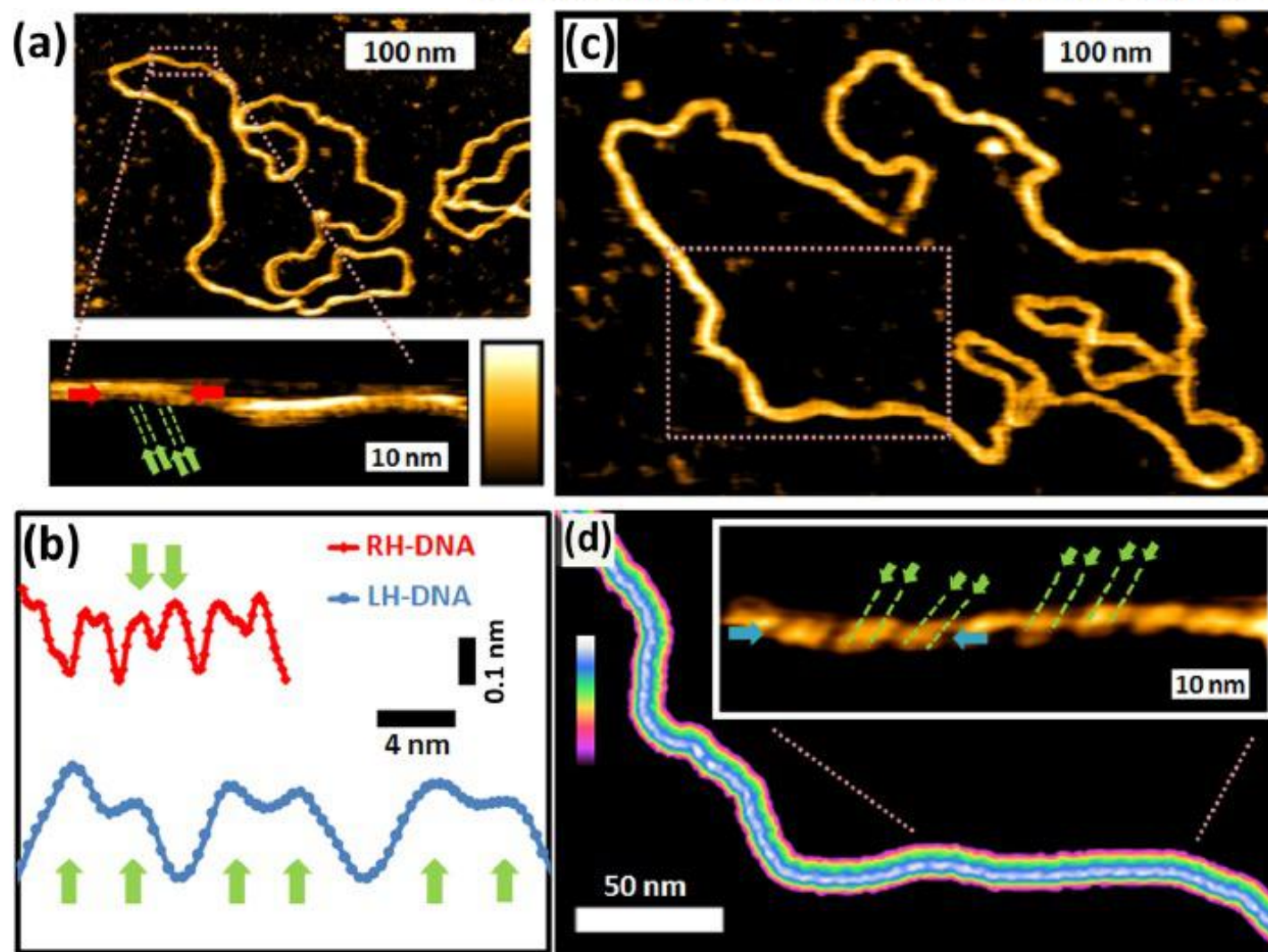
Figure 4. High-resolution AFM on plasmid DNA. (a) 3486 bp plasmid DNA, which on magnification shows a right-handed double helix, superposed to substantial height differences on and along the DNA. (b) Profiles along right-handed (RH) and left-handed (LH) DNA, acquired along the lines marked by the red and blue arrows in the insets of A and D. (c) Elongated configuration of the 3486 bp plasmid DNA displayed at the same scale as part a. (d) On subsequent magnifications of the dashed rectangle in c, an elongated left-handed double helix is resolved. Color scale: 1.5 nm (a); 1.1 nm (a, inset); 1.5 nm (c); 1.1 nm (d); 0.7 nm (d, inset). Green arrows indicate the two strands of the double helix, separated by the minor groove (depth $\lesssim$0.1 nm). The major groove (depth ∼0.2 nm) separates the subsequent turns of the double helix.

DNA adhesion on mica

Courtesy of C. Rivetti

MICA

Biotite

tetrahedral
layer

octahedral
layer

M2   M1

4.64 A

K   (001)

(a)

b

c

Si^{4+}

Al^{3+}

K$^+$

O^{2-}

OH$^-$

(b)

b
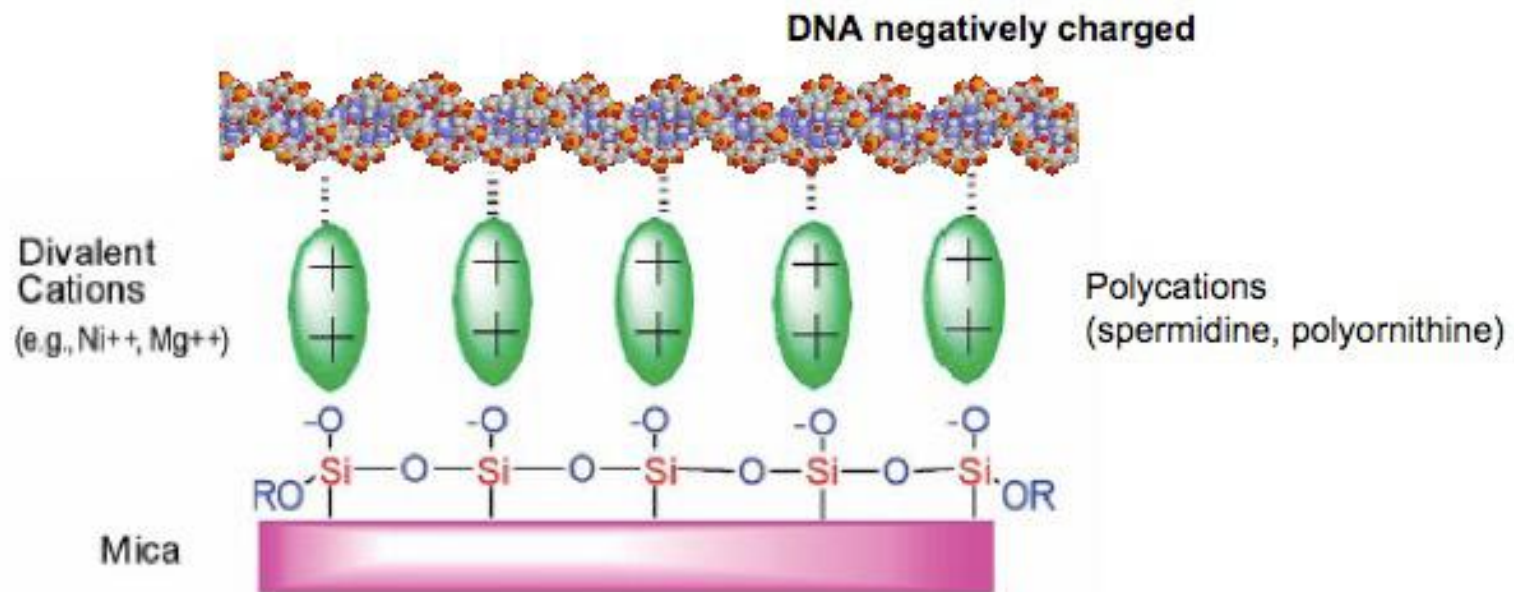
a
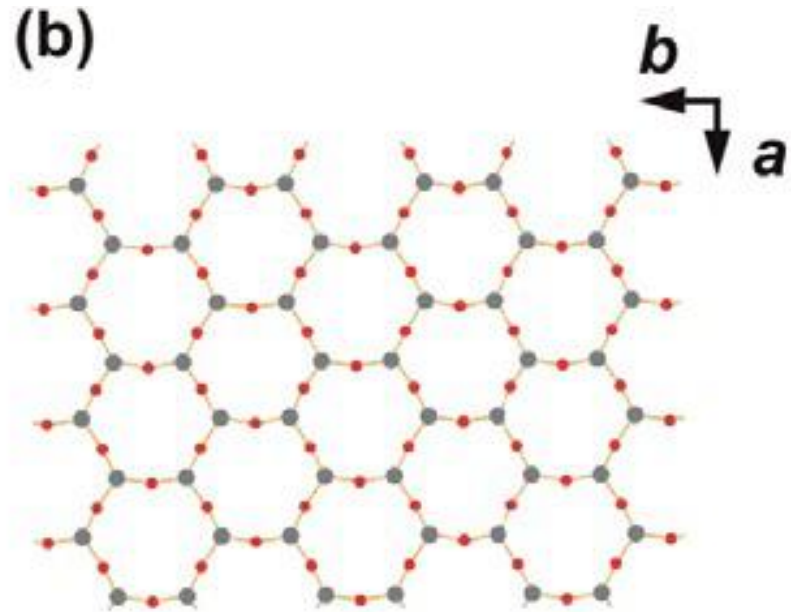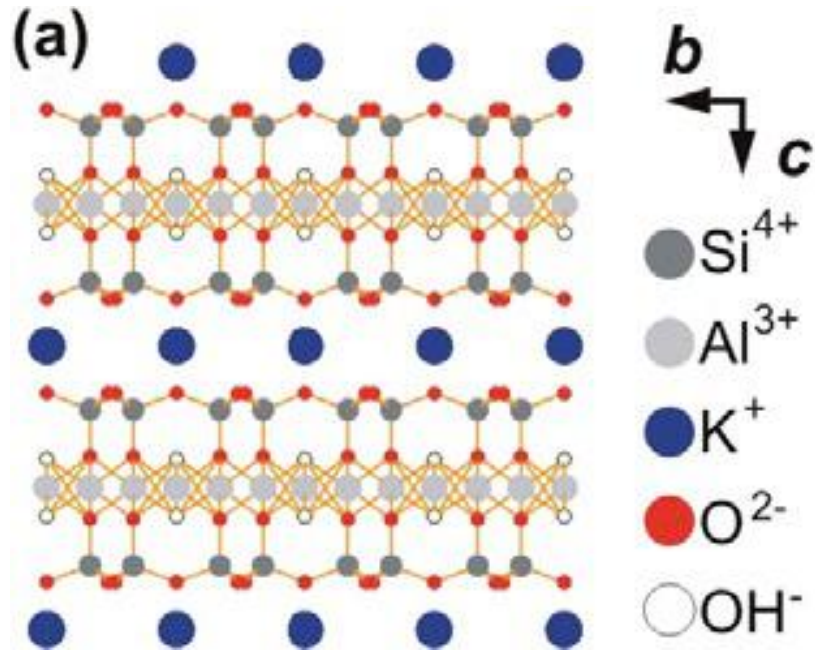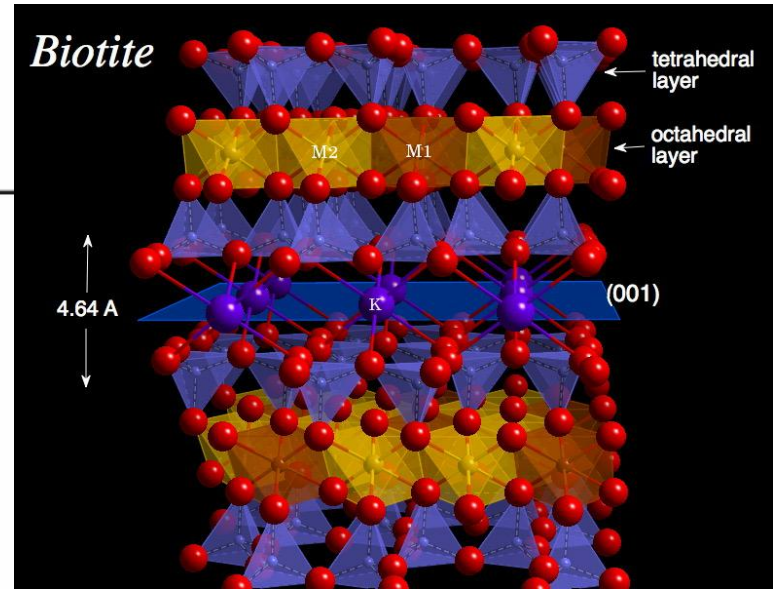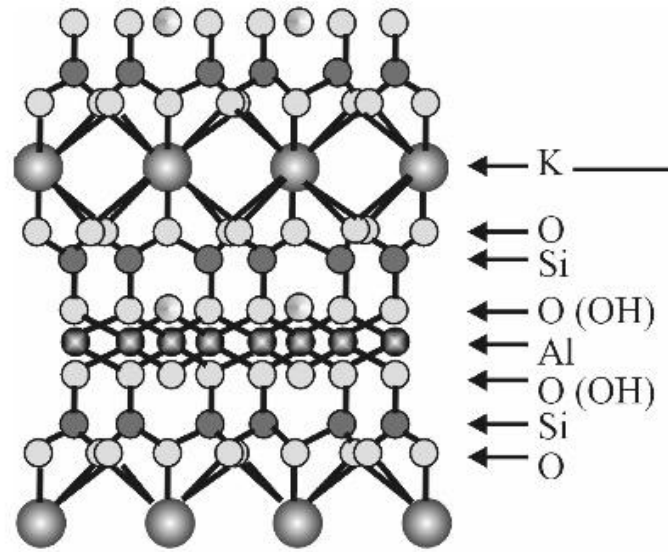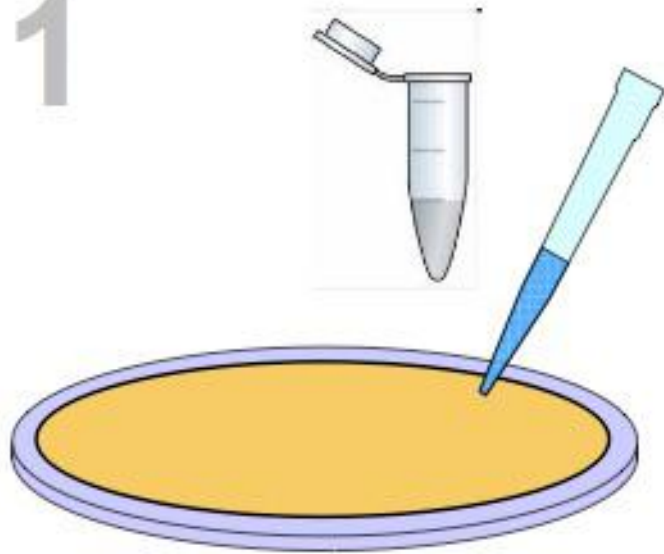
DNA deposition methods
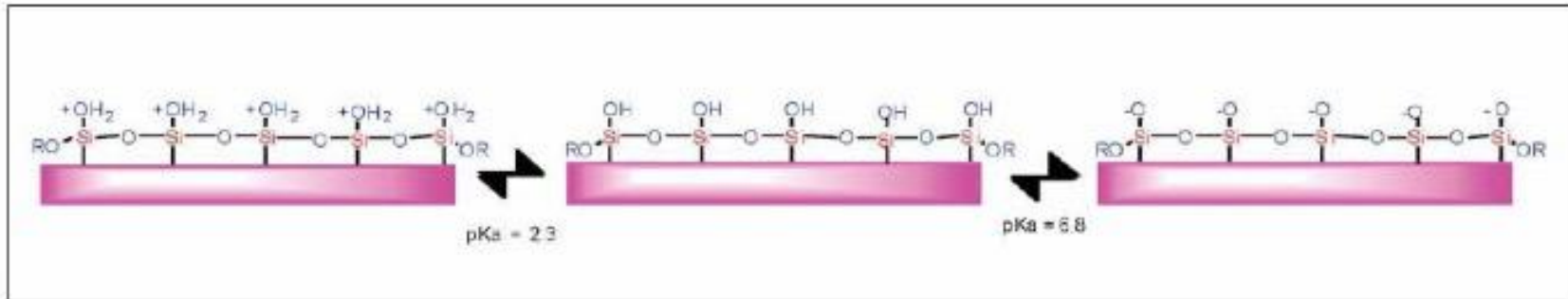
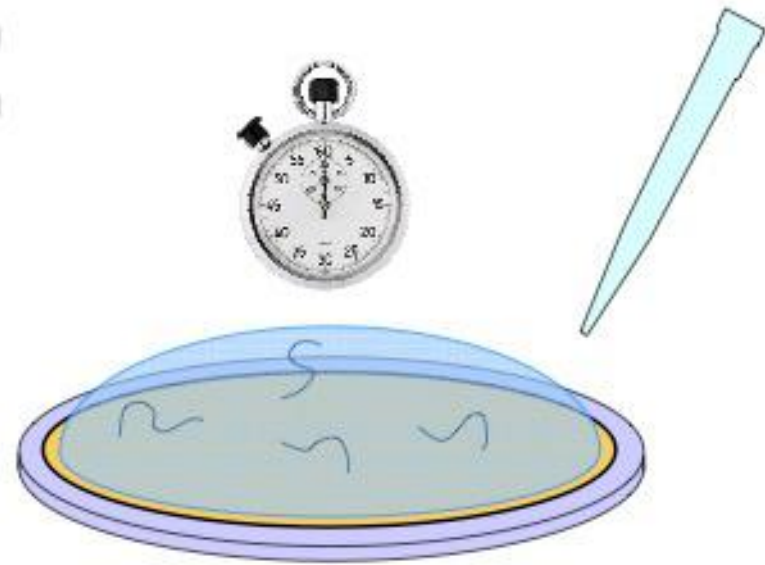Figure 1. Siloxy groups on the surface of freshly cleaved mica.
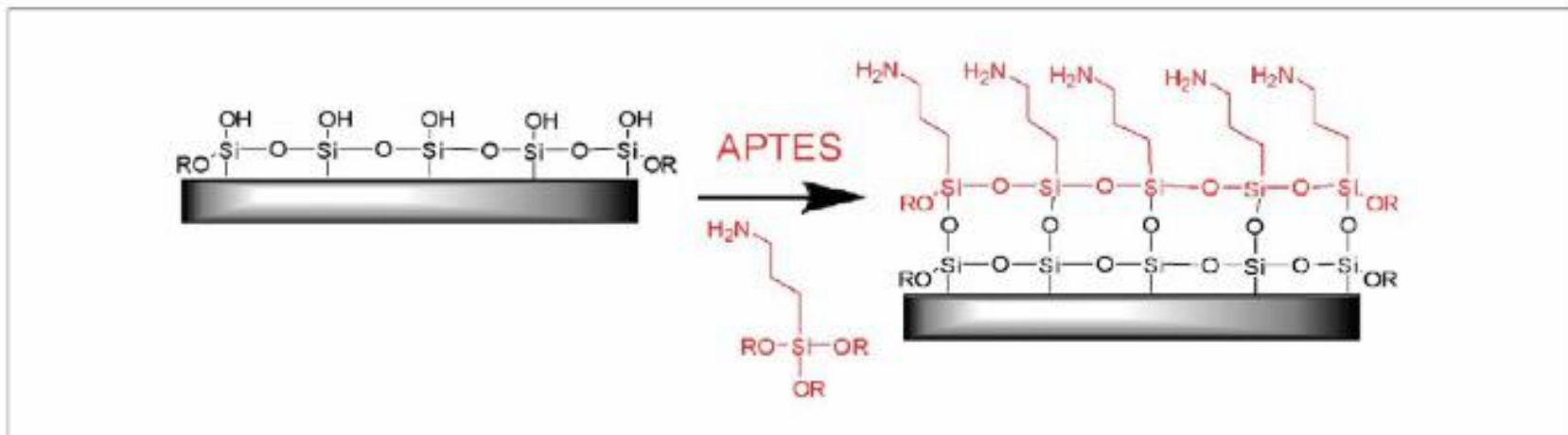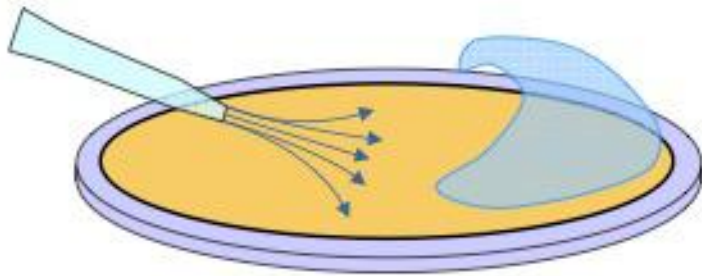

Figure 2. APTES treated mica substrate.

Courtesy of C. Rivetti

1

2

3

4

Courtesy of C. Rivetti
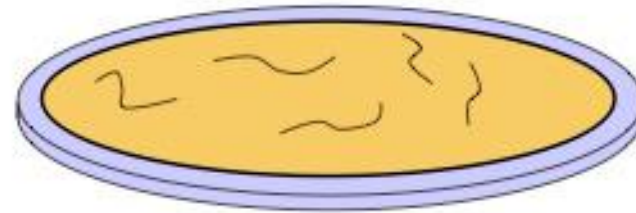
DNA deposition steps
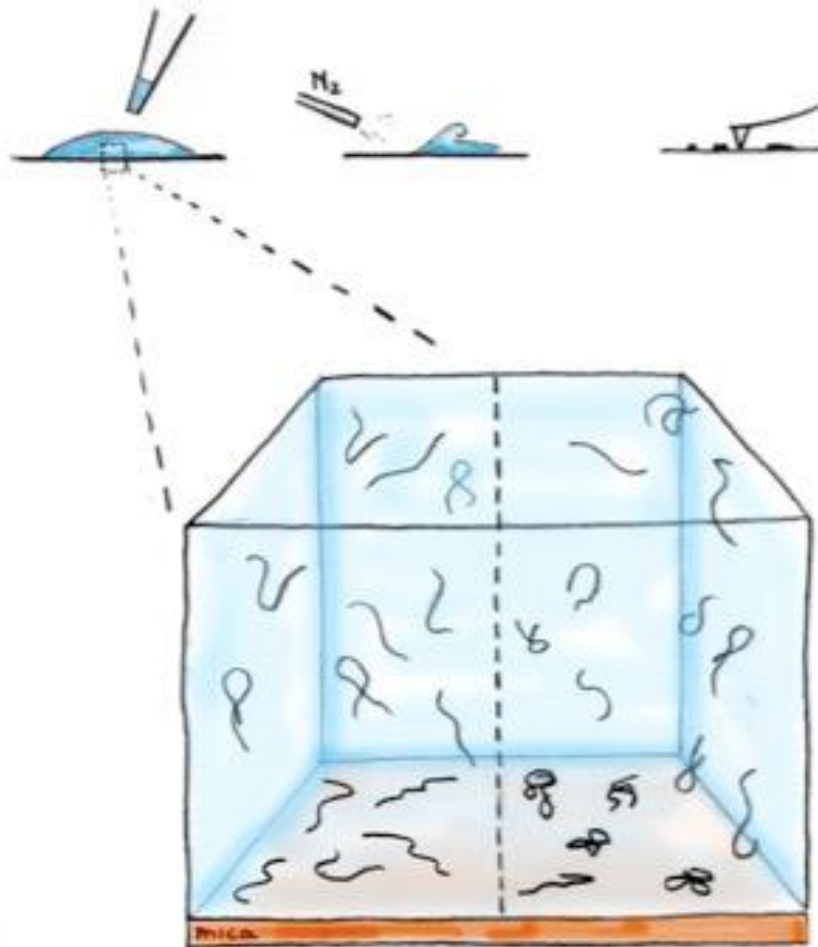
How do DNA molecules go from solution to the surface?

Once bound to the surface can they go back into solution?

What happens to the molecules on the surface before removing the buffer?
Can they move in 2D or are they trapped in a single conformation?

Can we quantitatively distinguish between the different cases?

Courtesy of Prof. C. Bustamante

DNA Deposition onto Untreated and Treated Mica

Freshly cleaved — Glow discharged — H⁺-exchanged
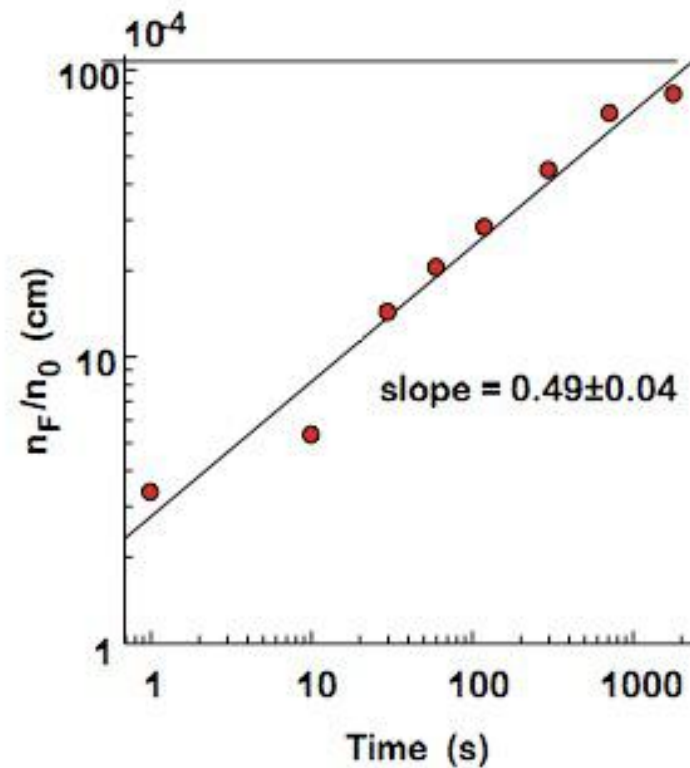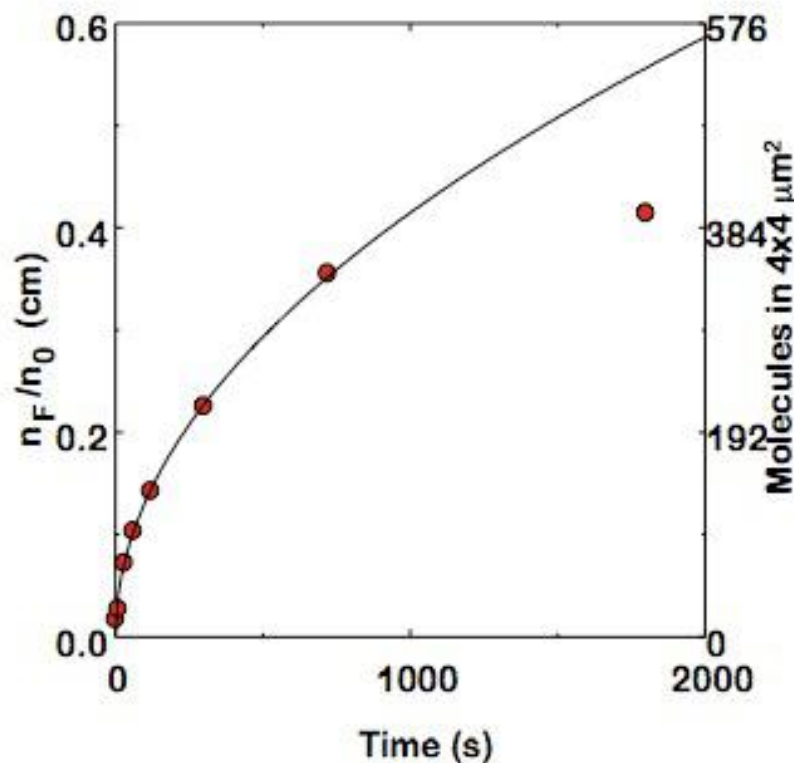
Courtesy of Prof. C. Bustamante
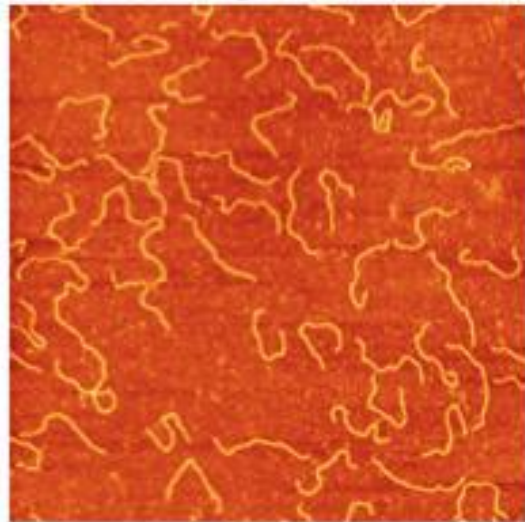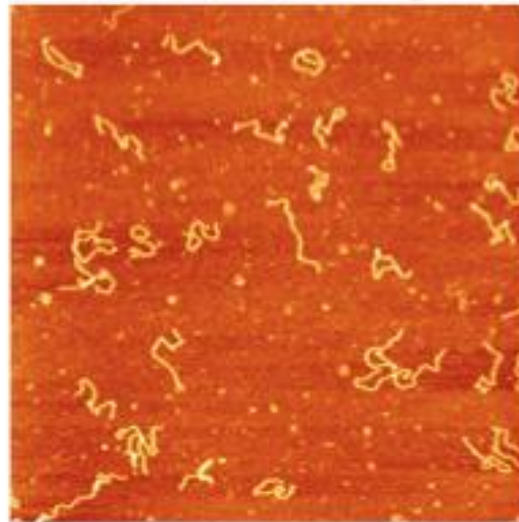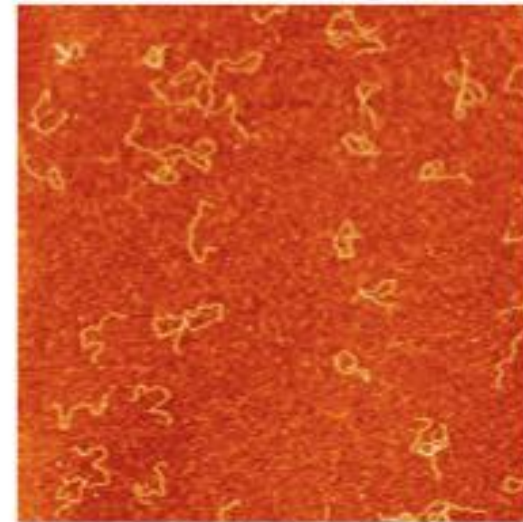
Number of DNA Molecules on the Surface vs. Time

On cleaved mica, transfer of DNA from solution to the surface is solely governed by diffusion:

n_0 initial DNA concentration in molecules/cm^3
D diffusion coefficient
t time of deposition

$$n_F = \frac{N.\ of\ Molecules}{Area} = \frac{2}{\sqrt{\pi}}\, n_0 \sqrt{Dt}$$

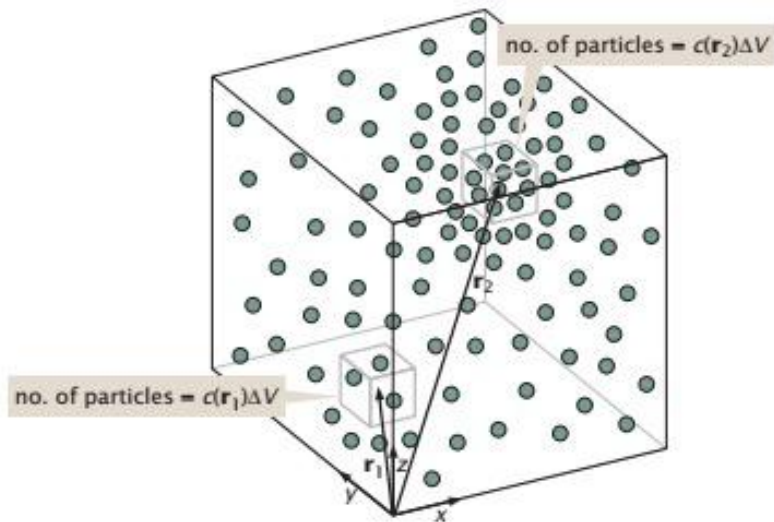slope = 0.49±0.04

$D = (5.4\pm0.2)10^{-8}\ cm^2/s$

Valid if:

- The molecules are irreversibly adsorbed to the surface
- Convection currents do not contribute to the transport of the molecules to the surface
- The solution is not significantly depleted of DNA molecules and the surface is not saturated during the time of deposition

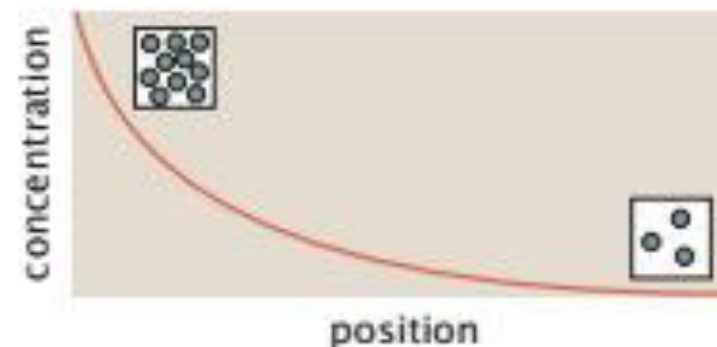Courtesy of Prof. C. Bustamante

Diffusive dynamics

we divide space up into a bunch of small boxes, large enough to include many molecules, but small enough so that the density is nearly uniform over the scale of the box.
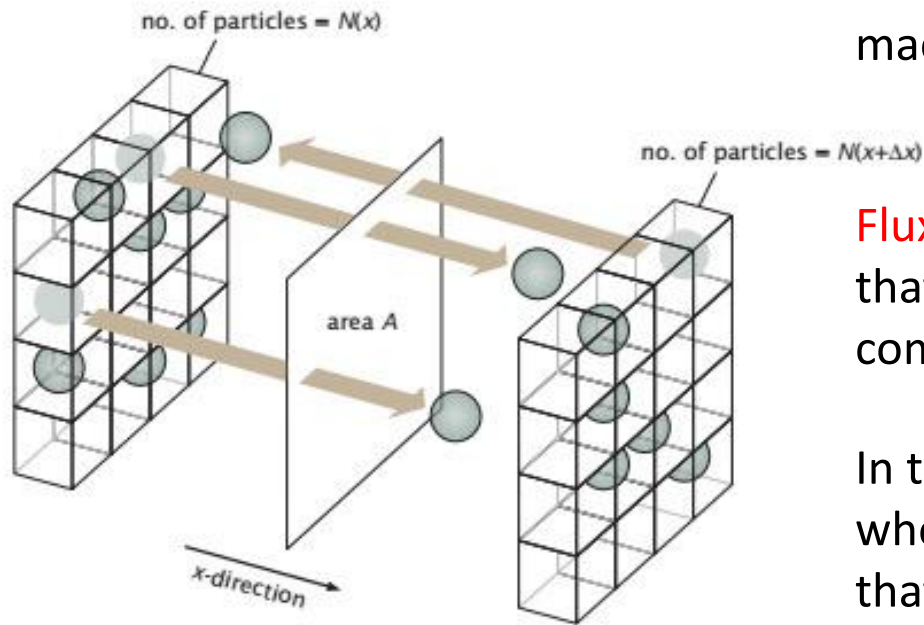
We use the notation c(**r**,t) to signify the concentration in a box centered at position **r** in three-dimensional space (with units of number of particles per unit volume) and c(x,t) to signify the concentration field in one-dimensional problems (with units of number of particles per unit length).

"Concentration gradient" is a spatial variation in the concentration field.

simple concentration profile where on the left-hand side of the domain of interest, the concentration of the molecule of interest is high, while on the right-hand side of the domain of interest, the concentration is low

Phillips, Rob; Kondev, Jane; Theriot, Julie; Garcia, Hernan. Physical Biology of the Cell (Page 516). CRC Press.

Diffusive dynamics

no. of particles = $N(x)$

no. of particles = $N(x+\Delta x)$

area A

x-direction

The other key quantity of interest for our macroscopic description of diffusion is the flux.

Flux can be seen as the net number of molecules that cross area A per unit time. That is the component of the flux vector in that direction.

In three dimensions, the flux is actually a vector whose components give the flux across planes that are perpendicular to the x-, y-, and z directions.

The goal of our thinking is to determine what amounts to an "equation of motion" that tells how the concentration field changes in both space and time.

Diffusive dynamics

in one dimension, flux is linearly related to concentration gradient:

$$j = -D\frac{\partial c}{\partial x},$$

(13.1)

J = current density, number of particles crossing unit area/ unit time
D = diffusion coefficient

$$[j] = \frac{1}{length^2 \times time},$$

$$\left[\frac{\partial c}{\partial x}\right] = \frac{number\ of\ particles/length^3}{length} = \frac{number\ of\ particles}{length^4}.$$

[D] = length^2/time, indipendent on dimensionality of space!

Equilibrium Statistic of a Worm-like Chain

Isotropic rod continuously flexible. The worm-like chain model is particularly suited for describing stiffer polymers, with successive segments displaying a sort of cooperativity: all pointing in roughly the same u_1 direction

at T=0 K, the polymer adopts a rigid rod conformation Is smoothly curved at RT
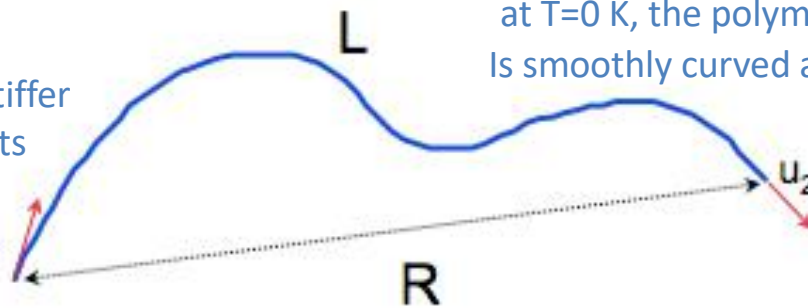
$$\langle \vec{u_1} \cdot \vec{u_2} \rangle = e^{-\frac{L}{P}}$$

The persistence length of the molecule, P, is the decay length through which the initial orientation of the molecule persist. It is a measure of the stiffness of a polymer chain.

In 2D the mean square end-to-end distance of a worm-like chain of length L, and persistence length P, is:

$$\langle R^2 \rangle_{2D} = 4PL \left(1 - \frac{2P}{L} \left(1 - e^{-\frac{L}{2P}} \right) \right)$$

For $L \to \infty$ $\langle R^2 \rangle_{2D} = 4PL$

Courtesy of Prof. C. Bustamante

WLC is for semi-flexible polymers.
Assumes polymers are inextensible, has a linear elastic bending energy and is subjected to thermal fluctuations.
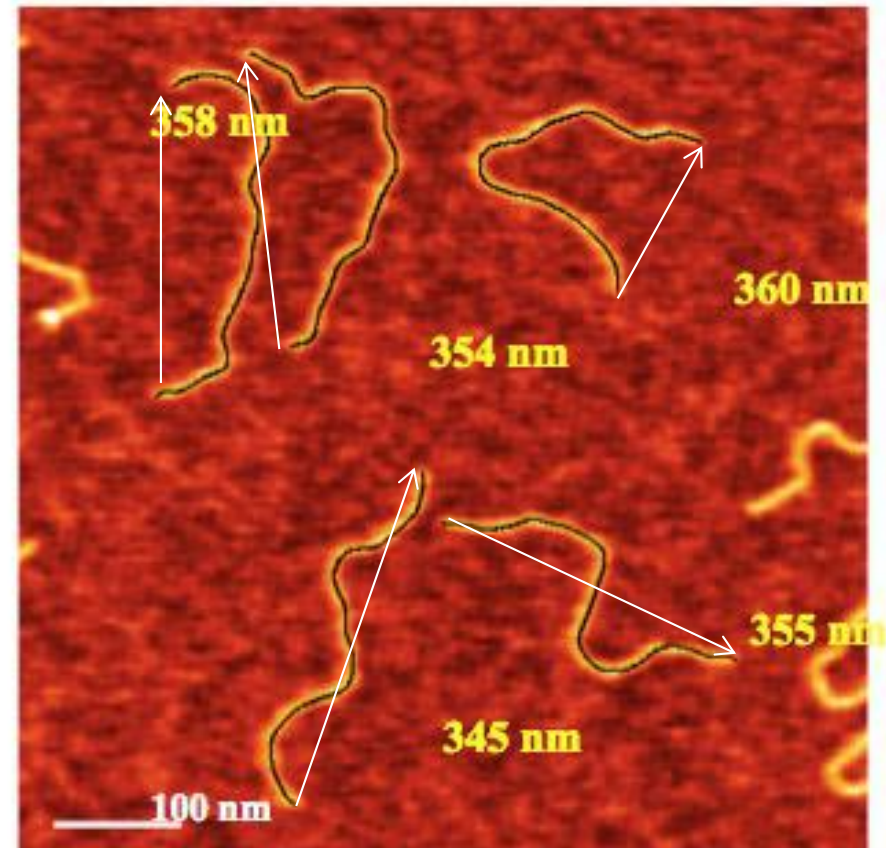
a) L=Nl segments, freely rotating

$$H = -\varepsilon \sum_{i=1}^{N-1} \vec{r}_{i+1} \cdot \vec{r}_i, \qquad (1)$$

which imposes an energy cost of $\varepsilon\ell^2$ times the cosine of the angle between neighboring segments. The right-hand side of (1) can be rewritten using the relation $\vec{r}_{i+1} \cdot \vec{r}_i = \frac{2\ell^2 - (\vec{r}_{i+1}-\vec{r}_i)^2}{2}$. Moving from a discrete model to a continuous model requires taking the limits $N \to \infty$ and $\ell \to 0$. Likewise:

$$\lim_{\ell \to 0} \left(\frac{\vec{r}_{i+1} - \vec{r}_i}{\ell} \right) = \frac{\partial \vec{t}(s)}{\partial s}, \qquad (2)$$

where $\vec{t}(s)$ is a tangent vector at location s along the contour of the polymer (see Fig. 1b). Finally, converting the sum to an integral yields:

$$\frac{H}{k_B T} = \frac{\xi}{2} \int_0^L \left(\frac{\partial \vec{t}(s)}{\partial s} \right)^2 ds, \qquad (3)$$
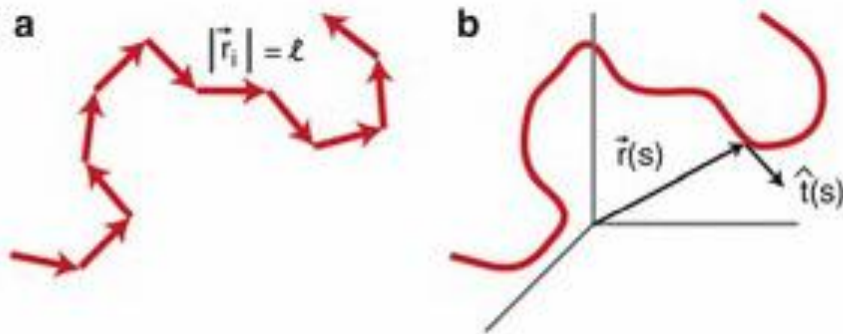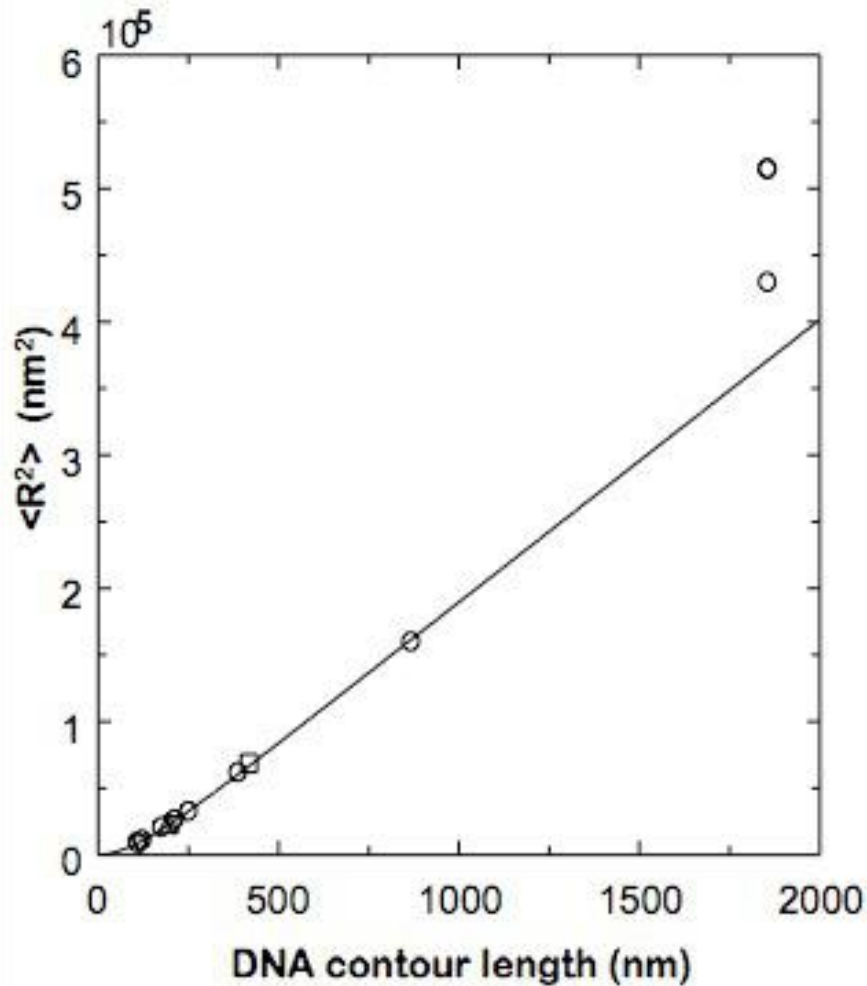

Worm-Like Chain (WLC) Model, Fig. 1 (a) Discrete model of a polymer composed of a chain of segments $\vec{r}_i$ each of length ℓ. (b) Continuous WLC polymer parameterized by the tangent vector $\vec{t}(s) = \frac{\partial \vec{r}(s)}{\partial s}$ along the contour

Adding energy cost associated to the bending:

WLC is for semi-flexible polymers.
Assumes polymers are inextensible, has a linear elastic bending energy and is subjected to thermal fluctuations.
a) L=Nl segments, freely rotating
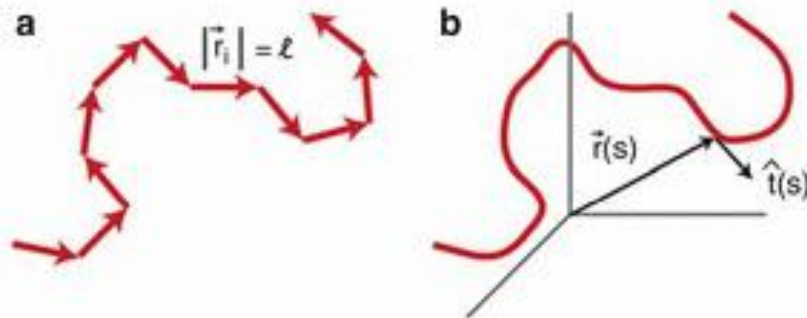
Worm-Like Chain (WLC) Model, Fig. 1 (a) Discrete model of a polymer composed of a chain of segments $\vec{r}_i$ each of length ℓ. (b) Continuous WLC polymer parameterized by the tangent vector $\vec{t}(s) = \frac{\partial \vec{r}(s)}{\partial s}$ along the contour

which is the Hamiltonian for the WLC model assuming that the contour length L is very large (Doi and Edwards 1988). Note the introduction of the persistence length $\xi = \frac{\epsilon \ell}{k_B T}$. The persistence length serves as a characteristic length scale over which two tangent vectors along the polymer remain correlated, i.e.:

$$\langle \vec{t}(s) \cdot \vec{t}(s') \rangle = e^{-\frac{|s-s'|}{\xi}}. \tag{4}$$

The WLC describes a polymer that is stiff over short distances and flexible at longer ones, with the persistence length setting the length scale of this transition in characteristic behavior. Moreover, while

Mean Square End-to-End Distance of DNA Molecules vs. their Contour Length

Courtesy of Prof. C. Bustamante and C. Rivetti

$$\langle R^2 \rangle_{3D} = 2PL\left(1 - \frac{P}{r}\left(1 - e^{-\frac{L}{P}}\right)\right)$$

$$\langle R^2 \rangle_{2D} = 4PL\left(1 - \frac{2P}{L}\left(1 - e^{-\frac{L}{2P}}\right)\right)$$

$$\langle R^2 \rangle_{proj} = \langle R_x^2 \rangle + \langle R_y^2 \rangle = \frac{2}{3}\langle R^2 \rangle_{3D}$$

Theoretical model for a 1258 bp DNA	$\langle R^2 \rangle$ nm^2
Ideal worm-like chain in 3D	35600
Ideal worm-like chain in 2D	60500
Orthogonal 3D → 2D projection	23700

$\langle R^2 \rangle = 61300$ nm^2 $\langle R^2 \rangle = 26000$ nm^2 $\langle R^2 \rangle = 25100$ nm^2
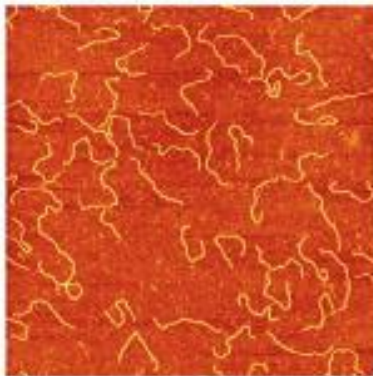
Freshly cleaved   Glow discharged   H$^+$-exchanged
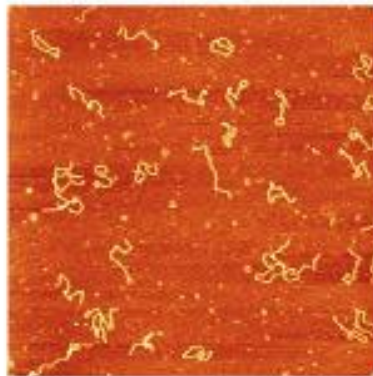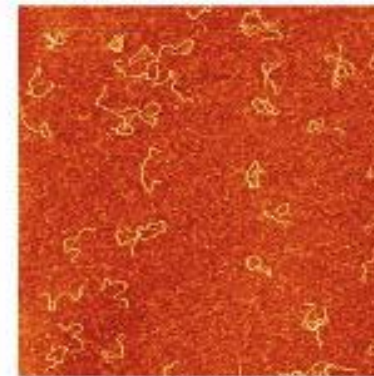
Courtesy of Prof. C. Rivetti

AFM under Liquid
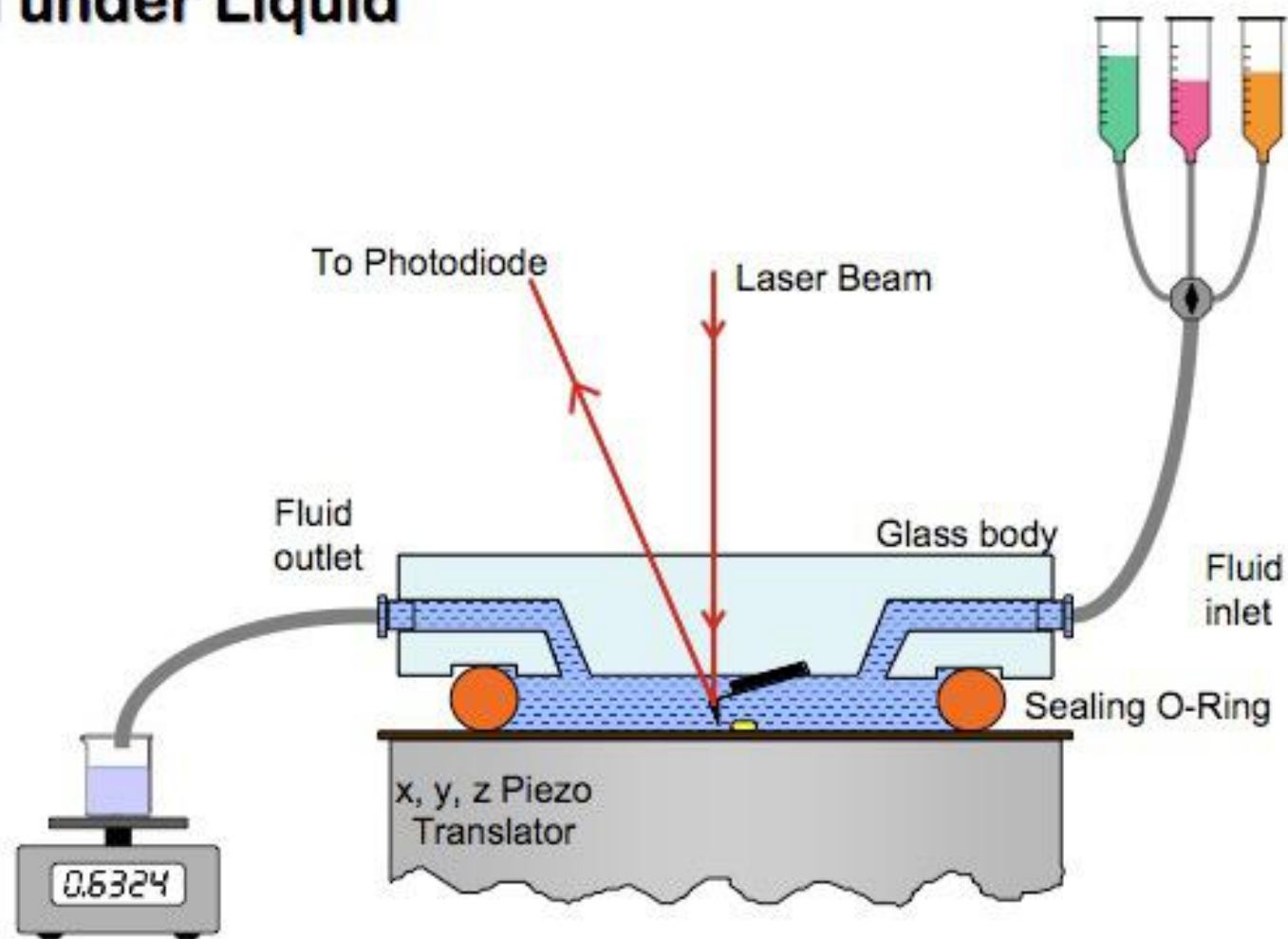
Courtesy of Prof. C. Rivetti

DNA imaged in liquid
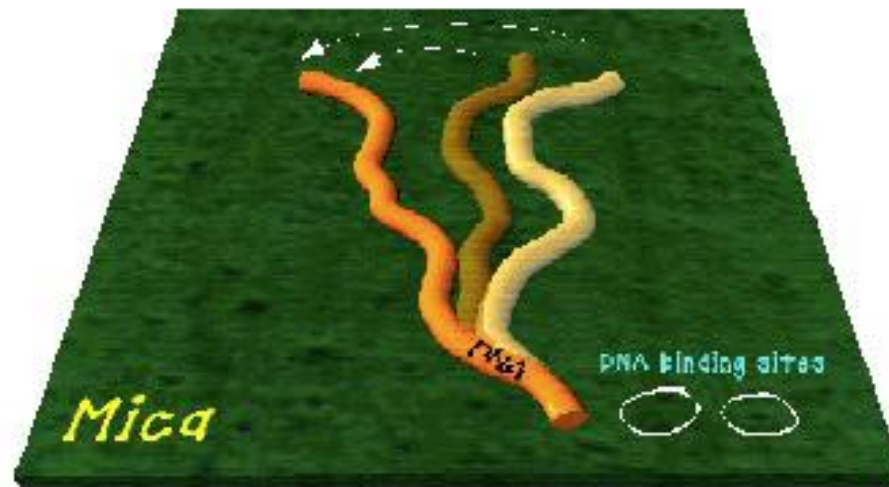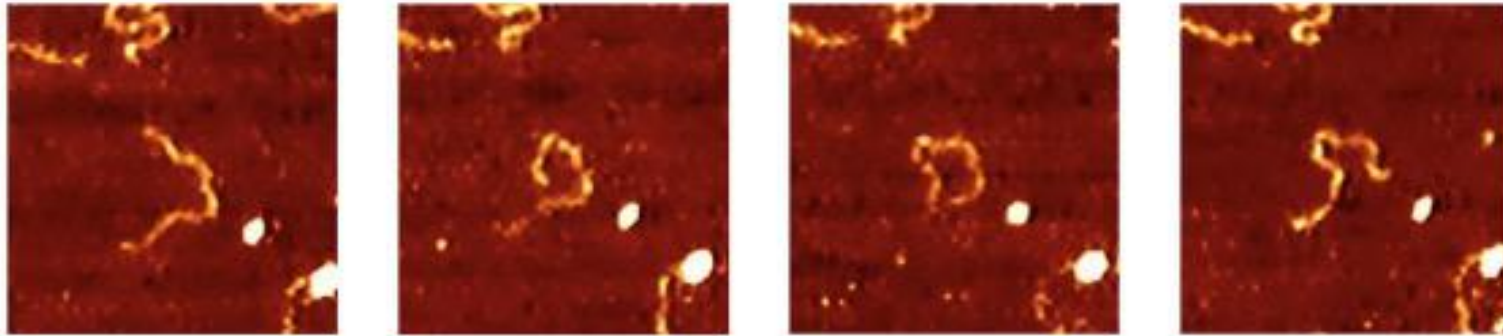
Courtesy of Prof. C. Rivetti

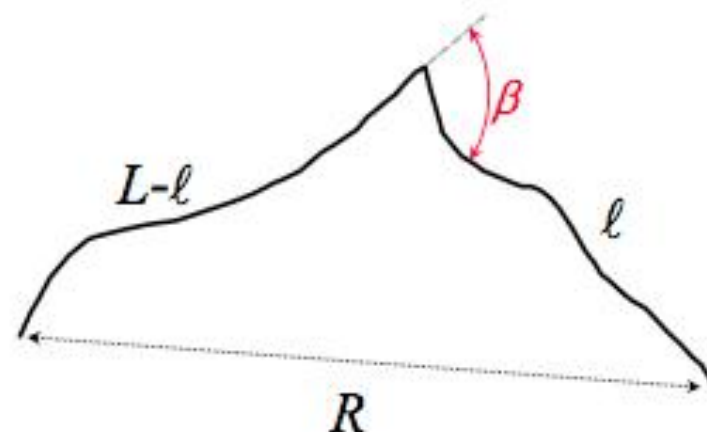# DNA bend angle measurements
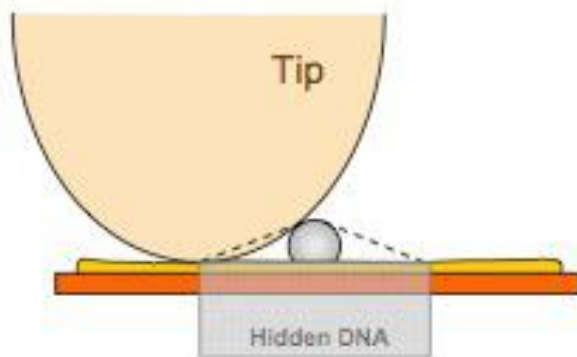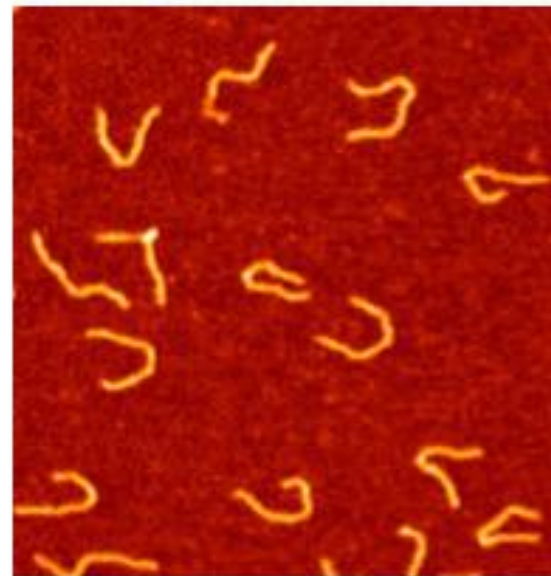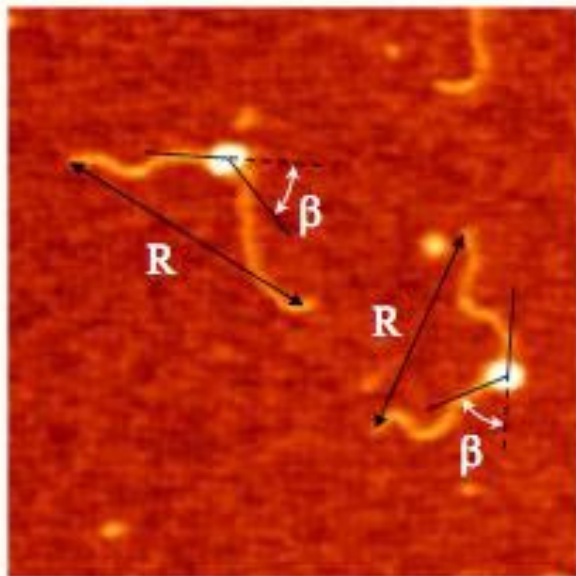
A-tract

10 bp
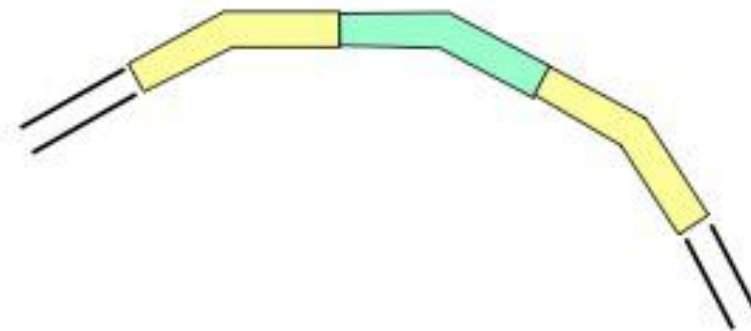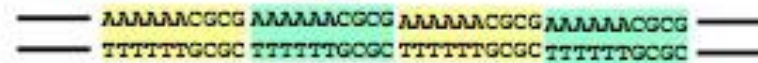
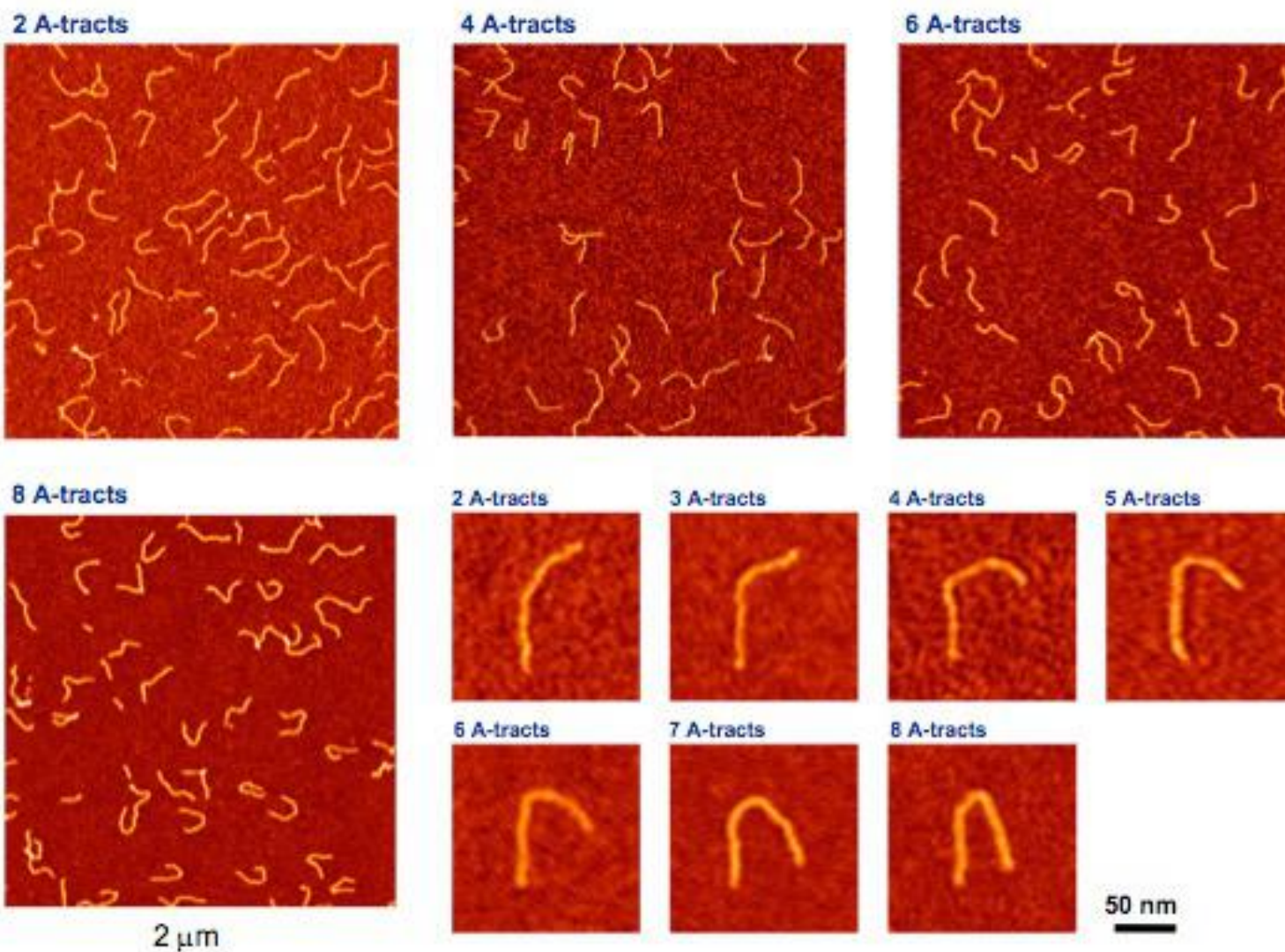## Using the end-to-end Distance to Determine Bend Angles

For a polymer molecule that is bent at any location along the chain, the mean square end-to-end distance is given by:
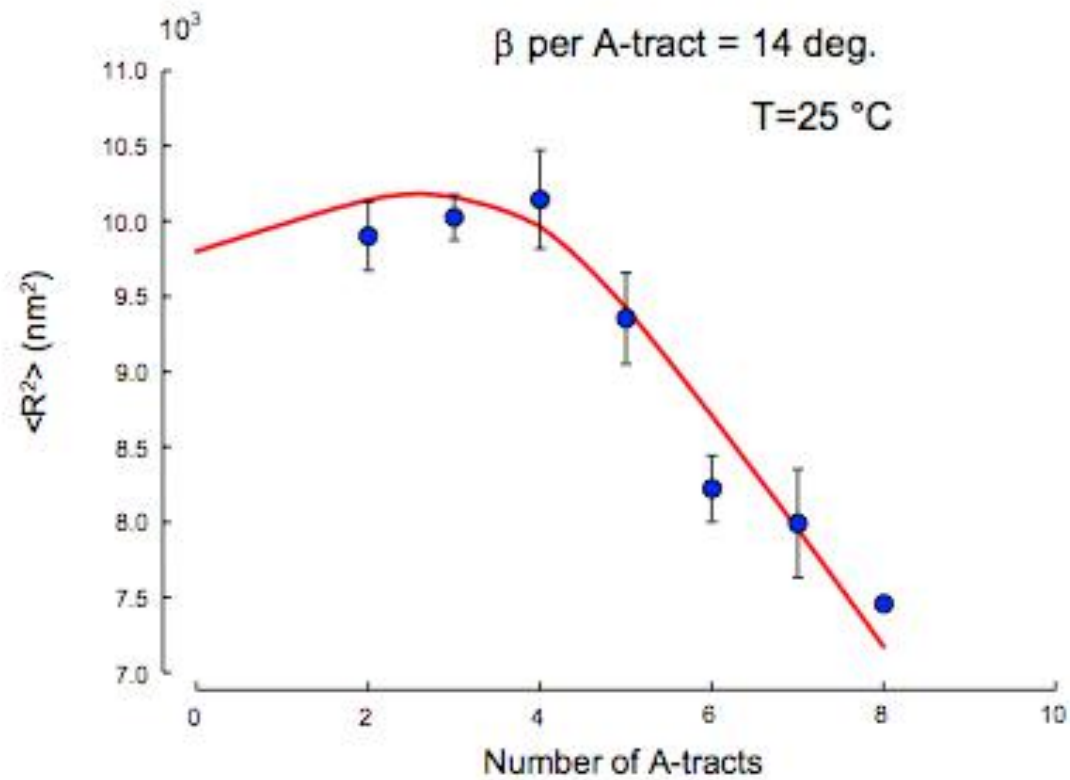

$$\left\langle R_\beta^2 \right\rangle_{2D} = 4PL\left\{1 - \frac{2P}{L}\left[\left(1-e^{-\ell/2P}\right)+\left(1-e^{-(L-\ell)/2P}\right)-\cos(\beta)\left(1-e^{-\ell/2P}\right)\left(1-e^{-(L-\ell)/2P}\right)\right]\right\}$$

DNA fragments containing A-tracts

2 A-tracts

4 A-tracts

6 A-tracts

8 A-tracts

2 A-tracts

3 A-tracts

4 A-tracts

5 A-tracts

6 A-tracts

7 A-tracts

8 A-tracts

2 μm

50 nm

Mean square end-to-end distance as a function of the number of A-tracts

Structure of the E. coli RNA Polymerase
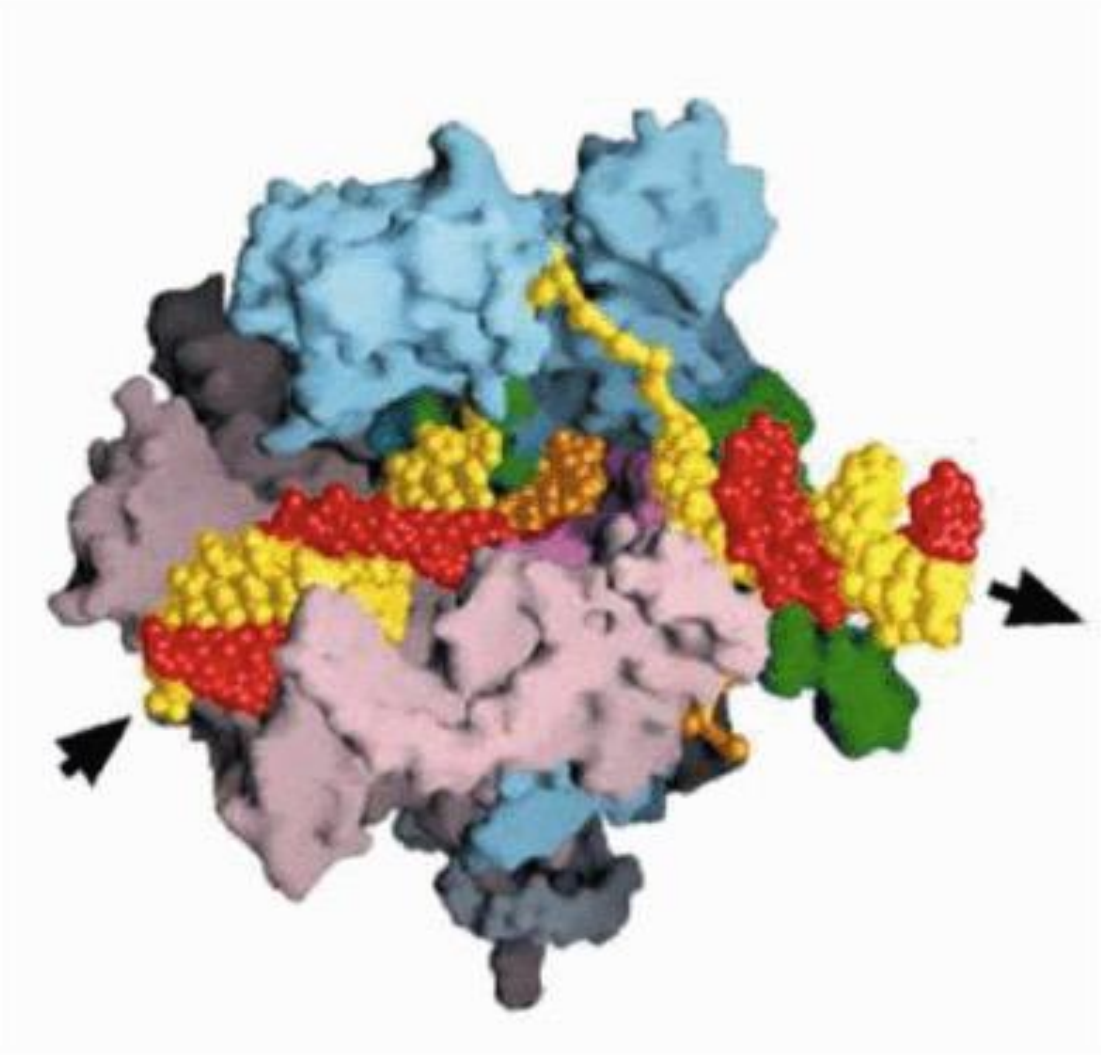
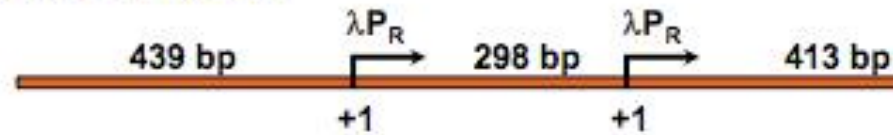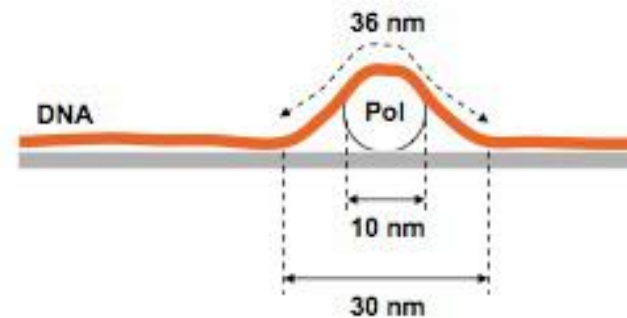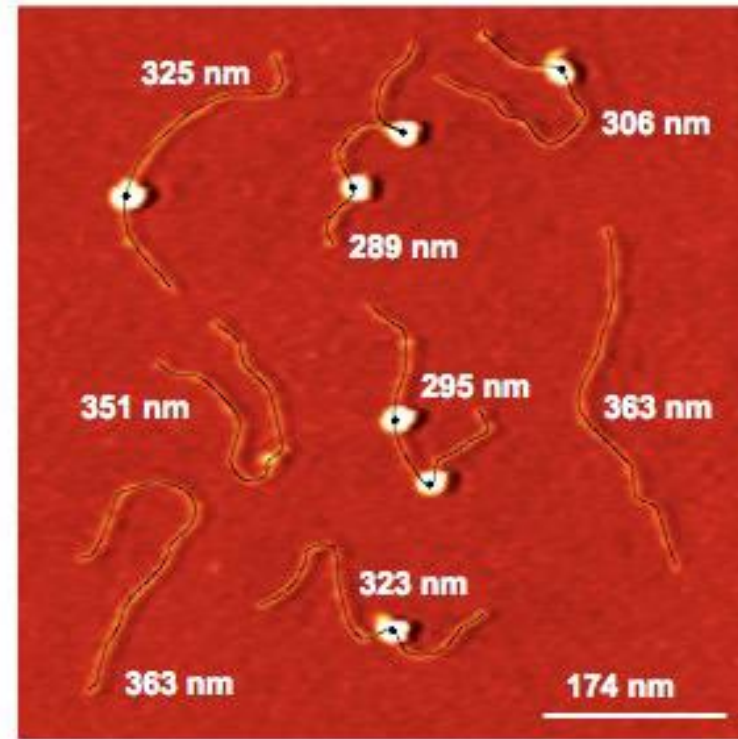Courtesy of Prof. C. Rivetti
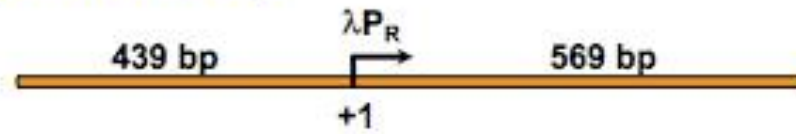
Courtesy of Prof. C. Rivetti

AFM image of Open Promoter Complexes

325 nm

306 nm

289 nm

351 nm

295 nm

363 nm

323 nm

363 nm

174 nm

280 nm

R
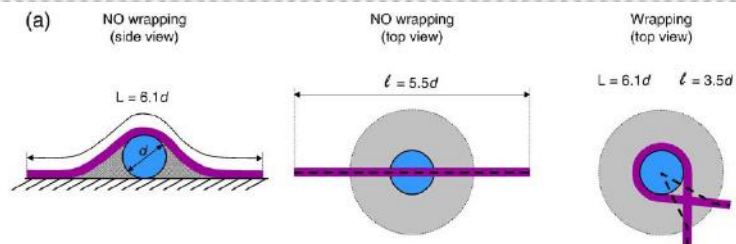
β

36 nm

DNA   Pol

10 nm

30 nm
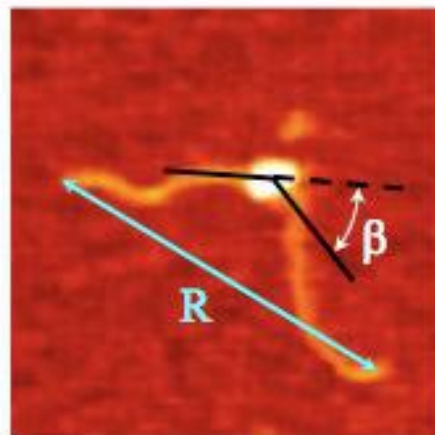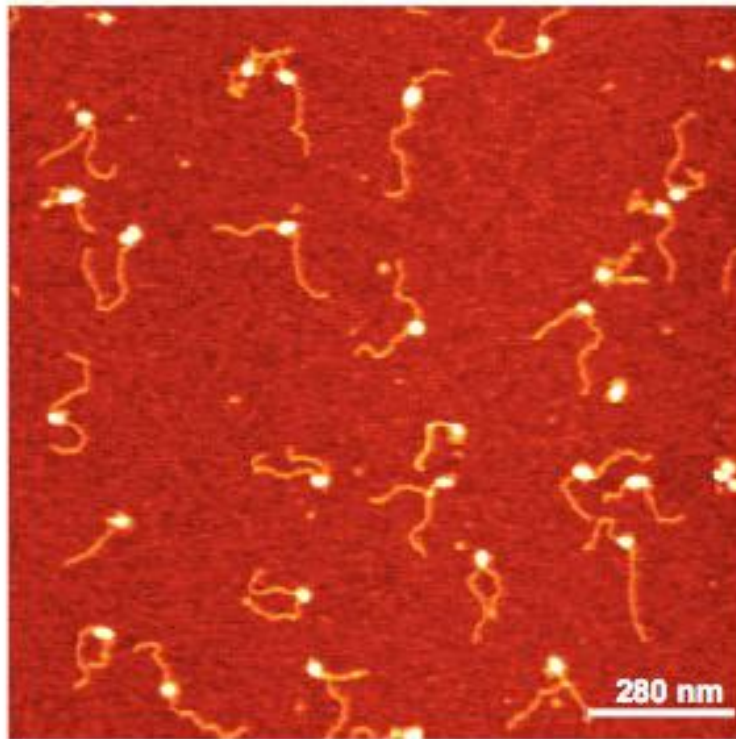
6 nm of DNA compaction

Courtesy of Prof. C. Rivetti

DNA Contour Length Measurements of Open Promoter Complexes
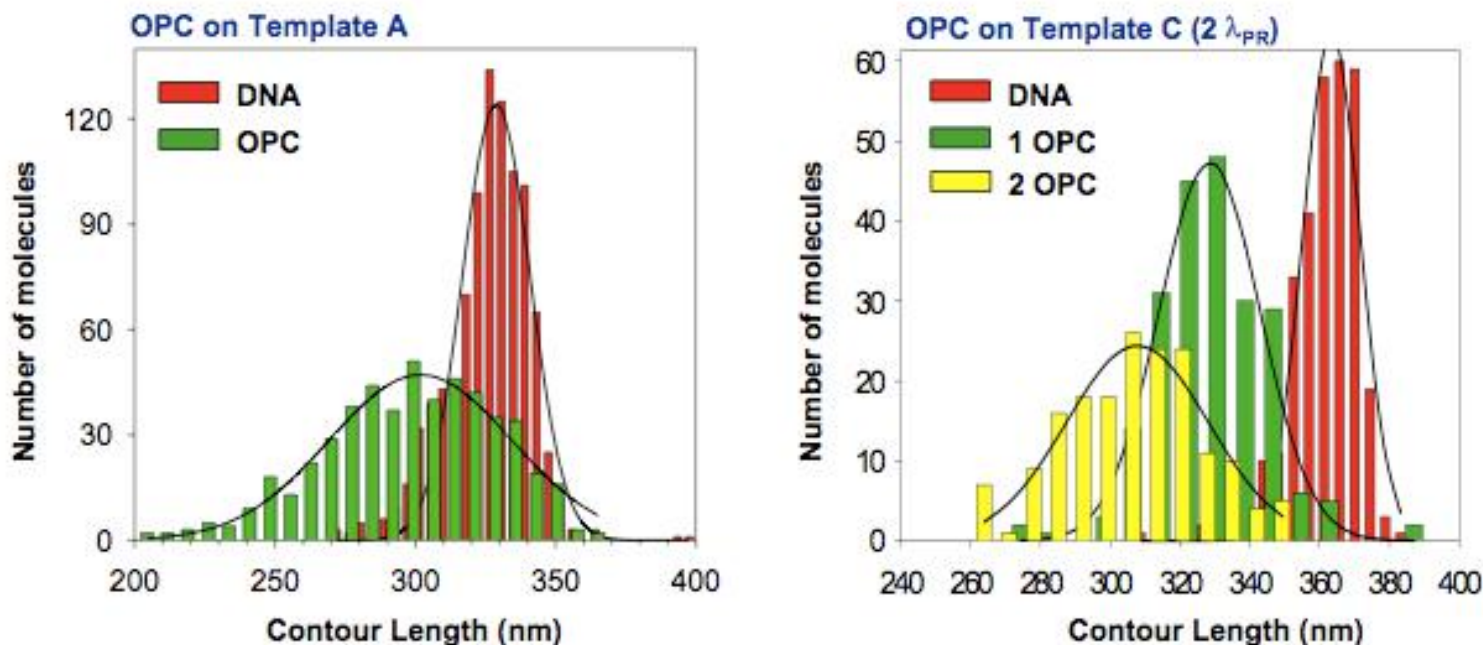
	Contour length (nm)	Compaction (nm)	N. of molecules
DNA (A)	329 ± 12		947
OPC (A)	297 ± 34	32	514
DNA (C)	363 ± 8		317
One OPC (C)	332 ±14	31	157
Two OPC (C)	308 ± 20	55	173

Proposed model for the open promoter complex at λ_{PR}

Courtesy of Prof. C. Rivetti